

2009-01-01

Characterization of high resolution range and Doppler chaotic LADAR

Berenice Verdin

University of Texas at El Paso, berever@miners.utep.edu

Follow this and additional works at: https://digitalcommons.utep.edu/open_etd



Part of the [Electrical and Electronics Commons](#)

Recommended Citation

Verdin, Berenice, "Characterization of high resolution range and Doppler chaotic LADAR" (2009). *Open Access Theses & Dissertations*. 378.

https://digitalcommons.utep.edu/open_etd/378

This is brought to you for free and open access by DigitalCommons@UTEP. It has been accepted for inclusion in Open Access Theses & Dissertations by an authorized administrator of DigitalCommons@UTEP. For more information, please contact lweber@utep.edu.

CHARACTERIZATION OF HIGH RESOLUTION RANGE AND DOPPLER
CHAOTIC LADAR

BERENICE VERDIN

Department of Electrical and Computer Engineering

APPROVED:

Benjamin C. Flores, Ph.D.

Virgilio Gonzalez, Ph.D.

Joseph Pierluissi, Ph.D.

Leticia Velazquez, PhD.

Patrick Debroux, PhD.

Patricia D. Witherspoon, Ph.D.
Dean of the Graduate School

Copyright ©

by

Berenice Verdin

2009

Dedication

With love to my daughter and husband
and
to my parents who have always encouraged me to follow my dreams

CHARACTERIZATION OF HIGH RESOLUTION RANGE AND DOPPLER
CHAOTIC LADAR

by

BERENICE VERDIN, MSEE

DISSERTATION

Presented to the Faculty of the Graduate School of
The University of Texas at El Paso
in Partial Fulfillment
of the Requirements
for the Degree of

DOCTOR OF PHILOSOPHY

Department of Electrical and Computer Engineering

THE UNIVERSITY OF TEXAS AT EL PASO

August 2009

Acknowledgement

This is the story of a little girl that had a dream. This dream began many years ago when she saw her father working hard to earn a PhD. At that time, this little girl began dreaming big, and visualized herself earning a PhD in Electrical Engineering. Now that dream is coming true...

I began working on this research four years ago. During that time, I have been blessed with many people that helped me to make this dream come true.

I want to offer my gratitude to my advisor Dr. Benjamin C. Flores. He has supported me for many years, patiently paving the way and sharing knowledge. He has enriched my growth as a student, a teacher, a researcher and a scientist.

I want to thank Dr. Patrick Debroux and Mr. James Boehm for their support on my research activities. In addition, I want to offer them my gratitude for the guidance and advice that they have given me to ensure the completion of this dissertation.

Last but not least I want to thank my family. They have always been and always will be the foundation of my life and the inspiration of my dreams.

Abstract

Compared to high range resolution radar systems, chaotic LADAR (laser detection and ranging) has the potential of providing an increase in range-Doppler resolution by several orders of magnitude.

The purpose of this project is to determine system parameters and signal processing schemes required to build a high resolution chaotic LADAR. Specifically, the LADAR is based on a semiconductor laser that generates a wideband chaotic signal via optical feedback. The behavior of the laser output is modeled by changing the control parameters of the delay differential equations that dictate the behavior of the laser output. Depending on the feedback level and the external cavity length the output of the laser, a route to chaotic behavior is found. Experiments show that the power spectral density and autocorrelation of the electric field of the laser output can be controlled for maximum range resolution. Further tests yield a process to optimize the entropy of the signal, autocorrelation sidelobe levels, Lyapunov exponent of the system and statistical properties of the signal. An ideal signal is obtained for a feedback level of 0.05 and an external cavity length of 0.30 m. The corresponding spectrum has a compression bandwidth of 22.12GHz.

In addition, a full analysis of the ambiguity function reveals that the optimized chaotic electric field has a “thumbtack shape” which is ideal for obtaining range and Doppler information. A range resolution of 6.7mm and a pedestal level -30dB is achieved. For illustrative purposes, the signature of a Boeing 777 is modeled using hot spots. The quality of the image is measured in terms of its entropy. Extremely low Doppler sidelobes are obtained.

Table of Contents

Acknowledgement	v
Abstract.....	vi
Table of Contents.....	vii
List of Tables	ix
List of Figures.....	x
Chapter 1: Introduction.....	1
1.1 Previous Work and Motivation.....	1
1.2 Goals and Methodology.....	2
Chapter 2: Theoretical Background.....	4
2.1 Chaotic Signals	4
2.2 Semiconductor Lasers.....	5
2.3 Semiconductor Laser with Feedback.....	7
2.4 Lyapunov Exponent.....	13
2.5 Power Spectrum, Autocorrelation and Ambiguity Function	15
2.6 Entropy Calculation	16
2.7 LADAR Principles.....	17
Chapter 3: Characterization of Chaotic Signal	24
3.1 Time Domain and Pseudo Phase Maps	24
3.2 Attractor of the System and Lyapunov Exponent.....	35
3.3 Time Series Properties.....	38
3.4 Power Spectrum and Autocorrelation.....	41
Chapter 4: Optimization of Control Parameters	49
4.1 Parameter Selection Approach	49
4.2 Statistical Properties of Chaotic Signal	49
4.4 Autocorrelation and Power Spectrum for Variable Feedback Level...56	
Chapter 5: LADAR Implementation	65
5.1 Optical Correlation	65
5.2 Ambiguity function.....	66
5.3 Target Imaging.....	70

Chapter 6: Conclusion	73
References.....	75
Vita... ..	77

List of Tables

Table 2.1: Parameters of Lang-Kobayashi equations	9
Table 2.2: Parameters of normalized Lang-Kobayashi equations	13
Table 2.3: Lyapunov exponents 3-D system	13
Table 3.1: Lyapunov exponents for different regimes.....	37
Table 3.2: Probabilistic and temporal statistical properties of electric field	39
Table 4.1: Four moments of the chaotic signal for variable external cavity length	50
Table 4.2: Four sample moments of chaotic signal for various feedback levels.....	51
Table 4.3: Main lobe width, poor man's Lyapunov exponent (LE) and bandwidth of chaotic field	54
Table 4.4: Autocorrelation main lobe width, poor man's Lyapunov exponent and bandwidth of electric field for variable η	60
Table 4.5: Evaluation of electric field for different feedback levels	63
Table 5.1: Entropy measurement for variable feedback level	70

List of Figures

Figure 2.1: Semiconductor laser structure.	6
Figure 2.2: Semiconductor laser with feedback.	8
Figure 2.3: LADAR basic block diagram.	18
Figure 2.4: Michelson interferometer used for autocorrelation.	19
Figure 2.5: Ideal ambiguity diagram.	22
Figure 3.1: Time behavior of periodic electric field.	25
Figure 3.2: Time behavior of intensity of laser output in the periodic regime.	26
Figure 3.3: Time behavior of mode hopping electric field.	27
Figure 3.4: Time behavior of intensity of laser output in the mode hopping regime.	27
Figure 3.5: Time behavior of chaotic electric field.	28
Figure 3.6: Time behavior of intensity of laser output in the chaotic regime.	29
Figure 3.7: Time behavior of carrier density in chaotic regime.	30
Figure 3.8: Time behavior of phase in chaotic regime.	30
Figure 3.9: Pseudo phase map of a random field.	32
Figure 3.10: Pseudo phase map of periodic field.	32
Figure 3.11: Pseudo phase diagram of chaotic field.	33
Figure 3.13: Pseudo phase map of carrier density in chaotic regime.	34
Figure 3.14: Pseudo phase map of phase.	35
Figure 3.15: Attractor of the system in the periodic regime.	36
Figure 3.16: Attractor of the system in the mode hopping region.	36
Figure 3.17: Attractor of system in the chaotic regime.	37
Figure 3.18: Probability density of electric field based on one realization.	40
Figure 3.19: Probability density of n^{th} sample of the electric field.	40
Figure 3.20: Bifurcation diagram for a fixed external cavity length.	41
Figure 3.21: Bifurcation diagram for a fixed feedback level.	42
Figure 3.22: Power spectrum of the electric field for the periodic regime.	43
Figure 3.23: Power spectrum of the electric field for the mode hopping regime.	44
Figure 3.24: Power spectrum of the electric field for the chaotic regime.	45
Figure 3.25: Autocorrelation of the electric field for the periodic regime.	46
Figure 3.26: Autocorrelation of the electric field for the mode hopping regime.	47
Figure 3.27: Autocorrelation of the electric field for the chaotic regime.	48
Figure 4.1: Autocorrelation of the electric field for $L_{\text{ext}}=0.05$ m.	52
Figure 4.2: Autocorrelation of the electric field for $L_{\text{ext}}=0.15$ m.	52
Figure 4.3: Autocorrelation of the electric field for $L_{\text{ext}}=0.30$ m.	53
Figure 4.4: Power spectrum of electric field for $L_{\text{ext}}=0.05$ m.	54
Figure 4.5: Power spectrum of the electric field for $L_{\text{ext}}=0.15$ m.	55
Figure 4.6: Power spectrum of the electric field for $L_{\text{ext}}=0.30$ m.	55
Figure 4.7: Autocorrelation of the electric field for $\eta=0.02$	56
Figure 4.8: Zoom in of the autocorrelation of the electric field for $\eta=0.02$	57
Figure 4.9: Autocorrelation of the electric field for $\eta=0.05$	57
Figure 4.10: Zoom in of the autocorrelation of the electric field for $\eta=0.05$	58
Figure 4.11: Autocorrelation of the electric field for $\eta=0.09$	59
Figure 4.12: Zoom in of the autocorrelation of the electric field for $\eta=0.09$	59
Figure 4.13: Power spectrum of the electric field for $\eta=0.02$	61
Figure 4.14: Power spectrum of the electric field for $\eta=0.05$	61

Figure 4.15: Power spectrum of the electric field for $\eta=0.09$	62
Figure 5.1: Schematic of the cross-correlation of the chaotic field.	65
Figure 5.2: Ambiguity function of the electric field of laser output.....	67
Figure 5.3: Zoom in of the ambiguity function of the electric field.....	67
Figure 5.4: Ambiguity function of intensity of laser output.....	68
Figure 5.5: Zoom in of ambiguity function of intensity.	68
Figure 5.6: Ambiguity function of the random signal.	69
Figure 5.8: Block diagram of bank of matched filters.....	71
Figure 5.9: Image of the target in the range and Doppler plane by using the electric field.	72
Figure 5.10: Image of the target in the range and Doppler plane by using the laser intensity.	72

Chapter 1: Introduction

The fundamental question we seek to address is whether a semiconductor laser system can produce a chaotic electric component of the electromagnetic electric field with nearly ideal characteristics for range-Doppler imaging applications. The working hypothesis is that feedback of the system, which is parameter dependent, can be adjusted to generate this chaotic electromagnetic field (signal). More specifically we seek to optimize a set of parameters that will produce a chaotic signal that upon processing yields optimum resolution in slant and cross range with minimal sidelobe interference.

1.1 Previous Work and Motivation

Ever since the first implementation of semiconductor lasers in 1962 [1], their opto-electronic characteristics have been widely studied. In 1980, Lang and Kobayashi discovered that by placing a partial mirror in front of a semiconductor laser as a mechanism for external optical feedback, its intensity begins to pulsate chaotically [2]. Lang and Kobayashi developed the theoretical model that is now used to study this type of behavior. For instance, Lenstra showed that the apparent temporal random behavior of the electromagnetic field forces the spectrum to spread its bandwidth well into the GHz range [3]. Massoller performed an analysis of the attractor and bifurcation diagram of the semiconductor laser system with feedback as the feedback level increases [4]. McInerney demonstrated that the coherence collapse state can be achieved via the period doubling route or by using a quasiperiodic route to chaos [5]. He performed an experiment to prove that the quasiperiodic route to chaos can be achieved when the oscillation frequency is not equal to a multiple of the external resonant frequency [6]. Ohtsubo proved that the route to the coherence collapse state is dependent on the external feedback reflectivity [7]. Mork performed a detailed analysis on the semiconductor laser system [8]. He demonstrated that the response depends on a characteristic parameter C that is proportional to the product of the feedback level and on the external cavity length. The parameter C is given by

$$C = \frac{\kappa\tau_{\text{ext}}}{\tau_{\text{in}}}\sqrt{1 + \alpha^2} \quad (1.1)$$

where κ is the feedback level, τ_{ext} is the external cavity round trip time, τ_{in} is the internal cavity round trip time and α the line width enhancement factor. In the case that $C < 1$ the frequency response of the laser output is essentially a spectral line. For $C > 1$ the frequency response of the laser is composed of two or more modes. For $C \gg 1$ the frequency response becomes unstable, entering into the coherence collapse state and producing a chaotic signal.

The potential use of chaotic lasers in LADAR applications has yet to be fully explored. Pethel, using an analog correlator demonstrated that the temporal correlation of the chaotic laser drops quickly, thus allowing for high resolution range measurements [9]. However, the characterization of the chaotic signal was limited to an experimental time sequence analysis. More recently, a chaotic LADAR was developed by Liu using a chaotic laser as the source. The chaotic signal was generated by using an optically injected semiconductor laser. He implemented detection and ranging using temporal correlation [10]. To date there is no evidence in the literature that a Doppler analysis has been conducted.

1.2 Goals and Methodology

As stated above, our working hypothesis is that the control parameters of the equations that govern the behavior of a semiconductor laser system with external optical feedback can be fine tuned to obtain high resolution in range and Doppler. For this purpose, we propose to perform a full analysis of the behavior of the laser's state variables as a function of two key control parameters, namely the external resonator spacing and mirror reflection coefficient. The complete characterization of the state variables (i.e. electromagnetic field amplitude and phase, and population inversion) will serve to prove that the waveform has a chaotic behavior. This characterization includes an in depth study of time iterations and strange attractors. Furthermore, the ergodicity of the system will be tested for infinitesimal variations in state variable initial conditions. We further propose to adjust and optimize the control parameters based on measurements of the Lyapunov exponent and entropy of the signal. Since

we envision that the signal processing will require a Michelson interferometer, we intend to model the matched filter as an optical correlator to obtain the simulations of autocorrelation and ambiguity function of the field, and thus determine the system's performance in the range and Doppler plane. Given the nature of the chaotic signal, this will include a statistical analysis of the ambiguity function. Finally, and for illustrative purposes, imagery of a multiple scattering point target will be generated by using the optimized chaotic signal.

Chapter 2: Theoretical Background

2.1 Chaotic Signals

The time behavior of a deterministic system is said to become chaotic when it evolves from a periodic to an aperiodic and apparently random behavior. Chaotic systems can be mathematically modeled by differential equations or, in the case of discrete systems, by difference equations. The governing equations of a chaotic system must be nonlinear and include at least three state variables. Otherwise, chaos cannot be induced. A solution of a difference equation is regarded as a sequence of iterates of some initial point [11]. Three descriptors are needed to characterize a chaotic system: the time evolution equations, the values of the parameters describing the systems, and the initial conditions. Chaotic systems are highly sensitive to initial conditions; a very small variation in initial condition produces a rather different signal. In addition, a small change in the control parameters can cause chaos to disappear or to reappear. The chaotic behavior of the system is quantified in terms of its Lyapunov exponents, which measure the degree of divergence of the state-space orbit of the system when it forms a strange attractor. Strange attractor is the geometrical manifestation of chaos in a nonlinear dynamical system.

Over the past two decades, chaotic signals have gained significant attention for telecommunication systems applications [12]. Specifically in radar applications, chaotic based generators are valuable alternatives for testing the vulnerability of radar systems to jamming signals. For instance, one-dimensional chaotic maps have been used to generate quasi-Gaussian signals for microwave radar applications [13, 14]. The effort was directed at finding the value of a control parameter that minimizes the sidelobes of the signal's temporal autocorrelation. In another study, Flores considered several one-dimensional maps to construct a frequency modulated signal with ideal ambiguity function properties [15]. The ambiguity function of the chaotic frequency-modulated (FM) signal was comparable to that of a Gaussian FM signal, which is often used as a standard of performance for random FM radar systems.

Given the ever increasing demands for higher range resolution capability and the need to deploy portable, low power detection and ranging systems, it is relevant to extend the study of chaotic systems well into the infrared or optical region of the electromagnetic spectrum. Of course, the analysis of chaotic laser systems becomes a priority. To date, there are three different schemes that can be used to generate a chaotic signal: optical injection, optoelectronic feedback and optical feedback [16, 17, 18]. Owing to the simplicity of the optical-feedback semiconductor system model we choose this approach for proof of concept.

2.2 Semiconductor Lasers

Semiconductor lasers are commonly used in optical applications since they offer a multitude of significant advantages, including small size, wavelength availability, power, and low cost. These lasers are often classified according to the wavelength of operation and the semiconductor elements that make up the cavity. For instance a popular semiconductor laser is made of GaAlAs and produces a wavelength from 500 nm to 1000 nm [19].

Essentially, a semiconductor laser is a p-n junction as shown in Figure 2.1. The p-type semiconductor material is reverse biased. Consequently, the electric field pushes the electrons in the n-region and the holes in the p-region toward the junction. When electrons and holes are in the same region they are recombined or annihilate. In the case that the electrons and photons are recombined they release energy in the form of photons [20].

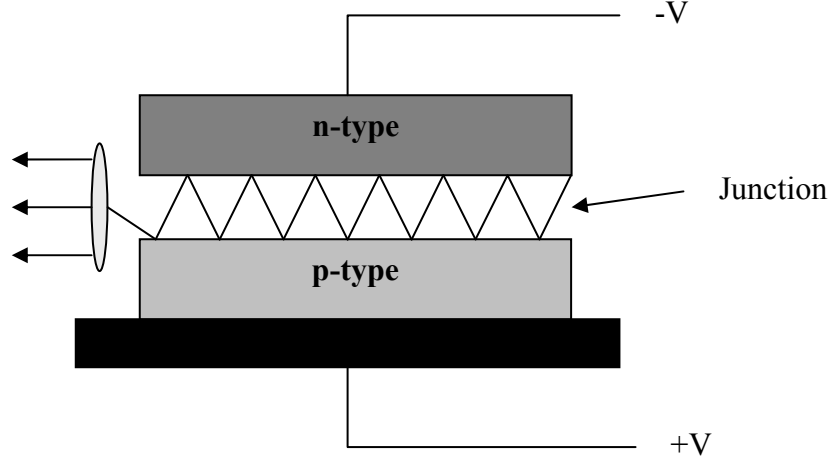


Figure 2.1: Semiconductor laser structure.

The electrical and optical performance of laser diode can be characterized by using the laser diode rate equations. The diode rate equations are a system of ordinary differential equations that relates the carrier density, the injection current and the diode material properties as carrier lifetime, optical gain and photon lifetime [21]:

$$\frac{dE(t)}{dt} = G_N(N - N_{th})E(t) + F_E(t) \quad (2.1)$$

$$\frac{d\phi(t)}{dt} = \frac{\alpha}{2}G_N(N - N_{th}) + F_\phi(t) \quad (2.2)$$

$$\frac{dN(t)}{dt} = J - \frac{N(t)}{\tau_s} - \left[\frac{1}{\tau_p} + G_N(N - N_{th}) \right] |E(t)|^2 + F_N(t) \quad (2.3)$$

where G_N is the differential gain, N is the carrier density, N_{th} is the carrier density at threshold, τ_s is the carrier lifetime, α is the linewidth enhancement factor, J is the pumping term, $F_E(t)$ is the photon number noise, $F_\phi(t)$ is the phase noise and $F_N(t)$ is the carrier density noise.

The noise induced in this system is mainly produced by spontaneous emissions of randomly excited atoms. This effect of such noise is observed in the amplitude and phase of the field [22]. In

equation 2.1, $F_E(t)$ is the representation of the Langevin noise associated with the electric field. The term $F_\phi(t)$ in equation 2.2 has an impact on the phase distribution. Likewise, the term $F_N(t)$ in equation 2.3 will have an impact on the carrier density. Both terms can be ignored when compared to $F_E(t)$. For the purposes of this study, all the terms of the Langevin noise are neglected.

The linewidth enhancement factor α that appears in equation 2.2 depends on the fluctuations in the real and imaginary components of the medium's refractive index. These fluctuations occur in the presence of spontaneous emissions as the system attempts to maintain the carrier density and electric field phase in a steady state. The linewidth enhancement factor is given by

$$\alpha = \frac{\Delta n}{\Delta n''} \quad (2.4)$$

where Δn is the change in the real part and $\Delta n''$ is the change in imaginary part (extinction coefficient) of the complex refractive index [23]. For semiconductors the value of α varies between 2 and 5.

Finally, the gain G_N which appears in equations 2.1-2.3 is defined as

$$G_N = \frac{\partial G}{\partial N} \quad (2.5)$$

which is the change of the gain with respect to the change in the carrier density.

2.3 Semiconductor Laser with Feedback

The semiconductor laser with external optical feedback is implemented by using a laser diode and a partial reflector (mirror) arranged as shown in Figure 2.2 [2].

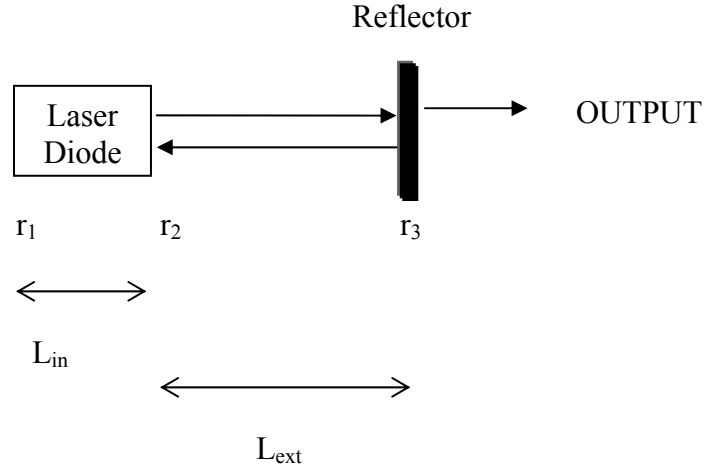


Figure 2.2: Semiconductor laser with feedback.

The laser diode cavity walls have internal reflectivity's r_1 and r_2 while the mirror placed at a distance L_{ext} from the laser has a reflectivity r_3 . A fraction of the electric field $E(t)$ that exits the laser is reflected back and enters the laser cavity. The reflected wave has an electric field $E(t-\tau_{ext})$ where $\tau_{ext}=2L_{ext}/c$ is the external round trip.

Since $E(t-\tau_{ext})$ is out of phase and interferes with the coherence of the field inside the resonator, the total field is strongly dependent to the feedback level, which depends on the reflectivity of the external mirror. The total field falls in several regimes, depending on the reflectivity of the external mirror k measured as a percentage [24]. For very small feedback ($0 < k < 1$), the laser is under single mode operation. For small feedback ($k \cong 1$) the laser undergoes mode hopping. For high feedback ($k > 10$), the laser becomes coherent again and the linewidth is narrowed. Our interest is in the moderate feedback regime ($1 < k < 10$) which produces a chaotic field with fluctuations in the time domain that can increase the laser linewidth from a few MHz up to 50GHz [3]. This coherence collapse is due to changes in the phase velocity of the waveform inside the cavity. Another way of obtain the range of the different regimes is by using the characteristic parameter C . So, for a fixed value of the external cavity length the characteristic value C can be obtained for different values of the feedback level.

The electric field and the carrier density of the system are modeled by using the Lang-Kobayashi equations that are obtained from the laser rate equations by adding the feedback term to equation 2.1 [3]. Thus the resulting state equations are

$$\frac{dE(t)}{dt} = \frac{1}{2}(1 + j\alpha)G_N(N(t) - N_{th})E(t) + \frac{k}{\tau_{in}}e^{-j\omega_0\tau_{ext}}E(t - \tau_{ext}) \quad (2.6)$$

$$\frac{dN}{dt} = J - \frac{N}{\tau_s} - \left[\frac{1}{\tau_p} + G_N(N - N_{th})\right]|E|^2 \quad (2.7)$$

Here $E(t)$ is the complex envelope of the electric field and $N(t)$ is the carrier density. Typical values for physical constants and parameters are listed in table 2.1 for reference.

Table 2.1: Parameters of Lang-Kobayashi equations

Symbol	Quantity	Value
τ_p	Photon lifetime	4.5 ps
τ_s	Carrier lifetime	700 ps
τ_{ext}	Round trip time in external cavity	1 ns
τ_{in}	Round trip time in laser cavity	3.9 ps
k^2	Power reflected from the external cavity	variable
α	Line width enhancement factor	5
J	Pumping term	2.38706×10^{27}
ω_0	Angular frequency of solitary laser	2.27×10^{15} rad.
N_{th}	Threshold carrier density of solitary laser	1.5×10^{18}
G_N	Differential gain	2.6×10^{-6}

The Lang-Kobayashi dynamical system can be tailored to explicitly show three state variables equations by specifying the amplitude and phase terms of the complex envelope of the electric the field:

$$E(t) = A(t)e^{j\varphi(t)} \quad (2.8)$$

Thus,

$$\frac{dE(t)}{dt} = \frac{d[A(t)e^{j\varphi(t)}]}{dt} = e^{j\varphi} \frac{dA(t)}{dt} + jAe^{j\varphi} \frac{d\varphi(t)}{dt} \quad (2.9)$$

Making the corresponding substitution in equation 2.6 and manipulating its real and imaginary parts will result in the following pair of differential equations:

$$\frac{dA(t)}{dt} = \frac{1}{2}G_N(N(t) - N_{th})A(t) + \frac{k}{\tau_{in}}A(t - \tau_{ext})\cos(\varphi(t) - \varphi(t - \tau_{ext}) + \omega_0\tau_{ext}) \quad (2.10)$$

$$\frac{d\varphi(t)}{dt} = \frac{1}{2}\alpha G_N(N(t) - N_{th}) + \frac{k}{\tau_{in}}\frac{A(t - \tau_{ext})}{A(t)}\sin(\varphi(t) - \varphi(t - \tau_{ext}) + \omega_0\tau_{ext}) \quad (2.11)$$

The system of equations above is a three dimensional flow where the state variables are the amplitude of the electromagnetic field $A(t)$, its phase $\varphi(t)$, and the carrier density $N(t)$ [25]. For simulations purposes, the flow is converted to a non-linear iterated map of the form:

$$A(n+1) = f[A(n), \varphi(n), N(n)] \quad (2.12)$$

where $A(n)$ is the discrete amplitude of the electric field phasor, $\varphi(n)$ is its discrete phase, and $N(n)$ is the sampled carrier density which obeys the transformation:

$$N(n+1) = g[A(n), \varphi(n), N(n)] \quad (2.13)$$

Likewise, the discrete version of the phase is of the form:

$$\varphi(n+1) = k[A(n), \varphi(n), N(n)] \quad (2.14)$$

The system can be solved using a fourth order Runge-Kutta numerical integrator. The sampling frequency has to be chosen to ensure that the chaotic attractor is smooth and that the spectrum of the electromagnetic field is not aliased.

As a note it should be stated that a normalized version of the Lang- Kobayashi equations is commonly found in the literature. The dynamical system is defined in terms of the complex electric field Y and the excess carrier number Z [26] as a function of normalized time variable s :

$$\frac{dY}{ds} = (1 + jR)ZY + \eta Y(s - \theta) \exp(-j\xi) \quad (2.15)$$

$$T \frac{dZ}{ds} = P - Z - (1 + 2Z)|Y|^2 \quad (2.16)$$

where

$$Y = \sqrt{\frac{\tau_s G_N}{2}} E \quad (2.17)$$

$$Z = \left(\frac{\tau_p G_N}{2} \right) (N(t) - N_{th}) \quad (2.18)$$

$$s = \frac{t}{\tau_p} \quad (2.19)$$

$$P = \frac{\tau_p G_N N_{th}}{2} \left(\frac{J}{J_{th}} - 1 \right) \quad (2.20)$$

$$J_{th} = \frac{N_{th}}{\tau_s} \quad (2.21)$$

$$\eta = \kappa \frac{\tau_p}{\tau_{in}} \quad (2.22)$$

$$\theta = \frac{\tau_{ext}}{\tau_p} \quad (2.23)$$

$$\xi = \omega_0 \tau_{ext} \quad (2.24)$$

$$T = \frac{\tau_s}{\tau_p} \quad (2.25)$$

The normalized version of the Lang-Kobayashi equations can be rewritten as a function of three state variables the electric field Y , the phase φ and the carrier density Z by separating the phase of the amplitude in the electric field as follows

$$\frac{dA_N(s)}{ds} = Z(s)A_N(s) + \eta A_N(s-\theta) \cos(\varphi(s) - \varphi(s-\theta) + \omega_0 \tau_{ext}) \quad (2.26)$$

$$\frac{d\varphi(s)}{ds} = RZ(s)A_N(s) + \frac{\eta A_N(s-\theta)}{A_N(s)} \sin(\varphi(s) - \varphi(s-\theta) + \omega_0 \tau_{ext}) \quad (2.27)$$

Table 2.2 summarizes the parameters used for the normalized version the Lang-Kobayashi equations which are based on the values listed above.

Table 2.2: Parameters of normalized Lang-Kobayashi equations

Symbol	Quantity	Value
η	Feedback rate	variable
P	Injection current	1
τ_{ext}	Optical feedback delay	133
τ_p	Photon lifetime	4.5ps
τ_s	Carrier lifetime	700ps
R	Linewidth enhancement factor	5
T	Carrier to photon lifetime	155.5

2.4 Lyapunov Exponent

The Lyapunov exponent measures the divergence of a system's state orbit due to small changes in the initial conditions. A system with three variables will have three Lyapunov exponents $\lambda_1 > \lambda_2 > \lambda_3$ [27]. The largest Lyapunov exponent λ_1 determines if a system is chaotic. For the field of the semiconductor laser to be chaotic, the largest Lyapunov exponent must be positive. In the event that the largest Lyapunov exponent is less than zero the electric field approaches an equilibrium point. When the largest Lyapunov exponent is near zero the system will approach a periodic orbit or limit cycle. The Lyapunov exponents for each different type of attractor are shown in table 2.3

Table 2.3: Lyapunov exponents 3-D system

λ_1	λ_2	λ_3	Attractor
-	-	-	Equilibrium point
0	-	-	Limit cycle
+	0	-	strange (chaotic)

For high order maps the Lyapunov exponent can be approximated as [28]:

$$\lambda = \frac{1}{n} \ln \left(\frac{d_n}{d_0} \right) \quad (2.28)$$

where d_0 is the initial distance between the initial points of two neighboring orbits O_i and O_j ,

$$d_0 = |\rho_j - \rho_i| \quad (2.29)$$

and d_n is the distance between the orbits for the n th iteration,

$$d_n = |\rho_{j+n} - \rho_{i+n}| \quad (2.30)$$

In the particular case of 3-dimensional maps, the Lyapunov exponent can be calculated by using the following procedure [27]:

1. Start with an initial condition $E_{a0}, \varphi_{a0}, N_{a0}$. The initial condition has to be inside of the attractor. This is called the unperturbed orbit a.
2. Choose an second initial condition separated from the initial conditions of orbit a by d_0 in any direction $E_{b0}, \varphi_{b0}, N_{b0}$. This is called the perturbed orbit b.
3. Iterate the delay differential equations one time step for each set of initial conditions.
4. Determine the new separation between orbits d_1 . The separation is calculated by using $d = [(E_a - E_b)^2 + (\varphi_a - \varphi_b)^2 + (N_a - N_b)^2]^{1/2}$
5. Evaluate $\lambda_1 = \log(d_1/d_0)$ which is the local Lyapunov exponent.
6. Readjust the initial conditions of orbit b so the separation between the orbits is d_0
7. Repeat step 3 to 6 to obtain an average of the Lyapunov exponent.

In the case that the dynamical equations of the system are not known the Lyapunov exponent can be calculated by using the “poor man’s Lyapunov exponent”. The poor man’s Lyapunov exponent is equal to the inverse of the width of the main lobe of the autocorrelation function [27].

2.5 Power Spectrum, Autocorrelation and Ambiguity Function

One of the primary objectives is to generate a chaotic electromagnetic field that has a flat, wide spectral distribution. The power spectrum is calculated by obtaining the magnitude square of the Fourier transform of the time domain field [29]:

$$|X(f)| = \int_{-\infty}^{\infty} x(t)e^{-j2\pi ft} dt \quad (2.31)$$

Given the chaotic nature of the electric field, it is best to reduce the variance of the spectrum through an averaging procedure. This will be discussed in chapter 3.

A second objective is to generate a signal with an autocorrelation that has sidelobes as low as possible. Recall that the temporal correlation is used to determine the degree of similarity between the two signals. The autocorrelation is the correlation of a signal with itself. The correlation between a signal $x(t)$ and a reference $h(t)$ can be calculated by using equation 2.32 [29]:

$$R_{xh}(t) = \int_{-\infty}^{\infty} x(t)h(t - \tau) d\tau \quad (2.32)$$

Here τ is the correlation lag. Setting $h(t) = x(t)$ yields the autocorrelation of the signal. In the case is $x(t)=y(t)$ the correlation becomes the cross correlation $R_{xy}(t)$. The autocorrelation can be also obtained by computing the inverse Fourier transform of the power spectrum as it shown in equation 2.33 [29].

$$R_x(t) = \int_{-\infty}^{\infty} |X(f)|^2 e^{+j2\pi ft} df \quad (2.33)$$

A third objective of this work is to generate an electric field that upon processing yields optimum range and Doppler resolution. For this purpose, we make use of the ambiguity function $\chi(\tau, f_d)$ which can be viewed as the time-frequency correlation of the signal.

For narrowband signals, the ambiguity surface is the magnitude square of the ambiguity function and is given by [30]

$$|x(\tau, f_d)|^2 = \left| \int_{-\infty}^{\infty} s(t) \cdot s^*(t + \tau) \cdot e^{-j2\pi f_d t} dt \right|^2 \quad (2.34)$$

where τ is the time-delay associated with the time of flight, f_d is the Doppler frequency, and $s^*(t)$ is the complex conjugate of the transmitted signal.

2.6 Entropy Calculation

The concept of entropy is introduced to evaluate the statistical characteristics of the electric field. Consider a random variable x with a probability density function of $p(x)$, Shannon's entropy is defined as [31]

$$S = - \int_{-\infty}^{\infty} p(x) \log p(x) dx \quad (2.35)$$

In analogy to Shannon's entropy, the entropy of the field's temporal autocorrelation is defined as follows

$$S_R = - \sum_{i=1}^N \frac{|R_E|}{\sum_{i=1}^N |R_E|} \log \frac{|R_E|}{\sum_{i=1}^N |R_E|} \quad (2.36)$$

where, R_E is the autocorrelation of the electric field and N is the total number of samples in the autocorrelation. A low entropy of autocorrelation means that the autocorrelation has low disorder; high entropy means more disorder. The entropy of the signal can be computed by using equation 2.36. Since

a chaotic signal is being generated, high entropy of the signal is required so the signal has more disorder. Similarly, the entropy of the ambiguity surface associated with the field is defined as [32]

$$S_{\chi} = -\sum \sum I_{i,j} \log I_{i,j} \quad (2.37)$$

where

$$I_{i,j} = \frac{\chi_{i,j}}{\sum \sum \chi_{i,j}} \quad (2.38)$$

and $\chi_{i,j}$ is the ambiguity function where i is the row index and j is the column index.

2.7 LADAR Principles

In general, a LADAR system uses the same principle as radars. The difference between them is that LADAR systems transmits and detects laser beams instead of RF signals as radars do. The basic operation of a LADAR is as follows, a laser is directed toward the target, some of the light is reflected back to the LADAR receiver where it is analyzed and processed to obtain the range, velocity and direction of the target. In a particular case we can discuss a Doppler radar where the LADAR is used to measure the velocity of the target. When the light beam hits a target moving towards or away from the LADAR system the frequency of the light reflected off the target will be changed creating a Doppler shift. For instance, if the target is moving toward the LADAR, the reflected light will be at a higher frequency.

There are some lasers that are commonly used for this type of application that operates on the ultraviolet, visible and infrared regions of the electromagnetic spectrum. The advantage of using a LADAR is that it gives more resolution than typical radar systems.

The block diagram of a LADAR system is shown in Figure 2.3. A LADAR system is composed of the following main components [33]:

- A laser that will generate the light wave at certain frequency depending on the type of laser that is being used.
- A beam splitter is used to split the signal into two, one that goes into the transmitter and the other one that goes into the square law detector.
- The amplifier increases the amplitude of the signal.
- The transmit optics are used to transmit the signal to the atmosphere.
- The signal hits the target and is reflected back to the receiver optics.
- The square law detector is used to obtain the cross correlation. The input to the square law detector is the sum of the original transmitted signal and the received signal.

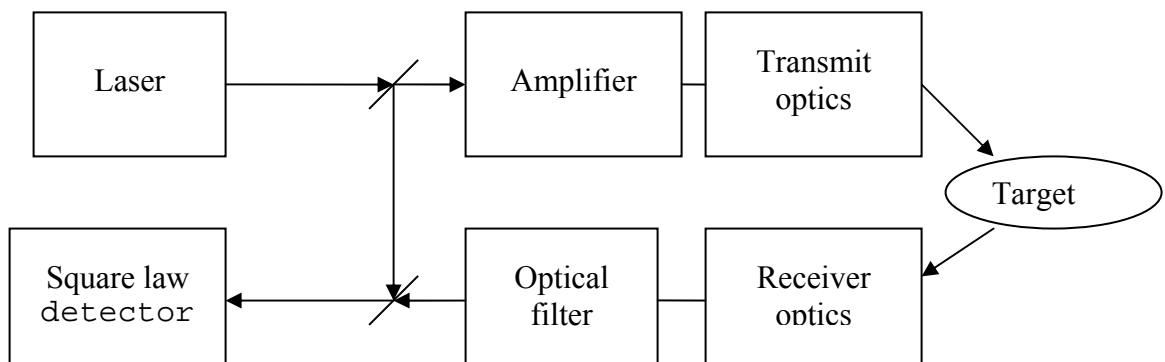


Figure 2.3: LADAR basic block diagram.

2.7.1 Optical Correlator

One of the main objectives is to obtain range and Doppler information of a target. The cross-correlation is used for obtaining the range information. Experimentally, the cross-correlation of the transmitted signal and the received signal can be obtained by using an optical interferometer. In this project, we propose to obtain the cross-correlation by using the Michelson interferometer that is shown in Figure 2.4 [34].

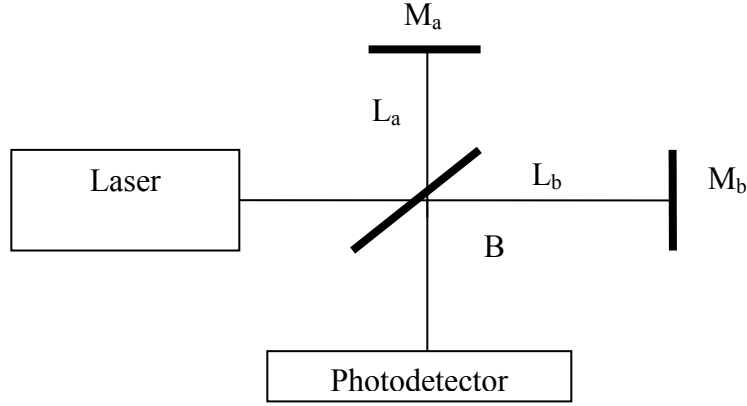


Figure 2.4: Michelson interferometer used for autocorrelation.

The electric field of the laser output is split into two waves by using the beam splitter B. The electric field $E_a(t-\tau_b)$ travels a distance L_b and then hits the mirror M_b . After that, the signal is reflected back with a delay τ_b given by

$$\tau_b = \frac{2L_b}{c} \tag{2.39}$$

where c is the speed of light. The electric field $E_a(t-\tau_a)$ travels a distance L_a and hits mirror M_a . The reflected electric field has a delay τ_a given by

$$\tau_a = \frac{2L_a}{c} \tag{2.40}$$

The distance L_b is maintained constant. However, the distance L_a changes with time to provide a variable delay line and evaluate the autocorrelation for different values of τ as

$$\tau = \tau_b - \tau_a \tag{2.41}$$

The photodetector detects the magnitude square of the addition of the two electric fields and since it is a slow detector only detects the cross term which has lower frequency than the other terms. The autocorrelation of the electric field is given by

$$R_E(\tau) = 2 \int_{-\infty}^{\infty} E(t)E^*(t - \tau)dt \quad (2.42)$$

In addition, the intensity cross-correlation can be obtained by using a second harmonic generator crystal placed before the photodetector. This second harmonic generator can be a lithium niobate crystal. This type of crystal has many applications as laser frequency doubling, nonlinear optics, and acousto-optic devices among others. In this research, this crystal is used as a second harmonic generator which is a nonlinear optical process. As a result, after the crystal the square of the sum of the electric fields is obtained $(E(t)+E(t-\tau))^2$. Since the photodetector only detects low frequencies it detects the cross-correlation of the intensity since the intensity is the magnitude square of the electric field

$$R_i(\tau) = \int_{-\infty}^{\infty} I(t)I(t - \tau)dt \quad (2.43)$$

2.7.2 Wideband Ambiguity Function

The wideband ambiguity surface, which finds use in the detection of high speed targets, is given by [35]

$$|x(\tau, \alpha)|^2 = \left| \alpha \int_{-\infty}^{\infty} s(t) \cdot s^*(\alpha(t + \tau))dt \right|^2 \quad (2.44)$$

Here α is the compression factor defined as

$$\alpha = \frac{c + v}{c - v} \quad (2.45)$$

where c is the speed of light and v is the radial velocity of the target toward the LADAR. Equation (2.44) can also be written as

$$|x(\tau, \alpha)|^2 = \left| \alpha \int_{-\infty}^{\infty} s(t - \tau) \cdot s^*(\alpha t) dt \right|^2 \quad (2.46)$$

Notice that for targets moving at non-relativist speeds, the frequency ratio $f_d/f_0 \ll 1$, so the compression factor can be approximated as

$$\alpha = \frac{f_d}{f_0} + 1 \quad (2.47)$$

where f_d is the Doppler shift and f_0 is the carrier frequency.

Let the transmitted signal be given by

$$s(t) = A(t)e^{j2\pi f_0 t} \quad (2.48)$$

Consequently, the compressed signal is given by

$$s\left[\left(1 + \frac{f_d}{f_0}\right)t\right] = A\left[\left(1 + \frac{f_d}{f_0}\right)t\right] e^{j2\pi f_0 \left(1 + \frac{f_d}{f_0}\right)t} \quad (2.49)$$

or

$$s\left[\left(1 + \frac{f_d}{f_0}\right)t\right] \approx A(t)e^{j2\pi f_0 t} e^{j2\pi f_d t} \quad (2.50)$$

This allows the wideband model to be replaced by the narrowband model.

The ideal ambiguity diagram is a two dimensional delta distribution on a pedestal of self noise otherwise known as a “thumbtack” function. This function does not have ambiguities in range or Doppler. However, this kind of pulse that produces an ideal ambiguity function is not physically realizable. A graphical example of the equation of the ideal ambiguity function is shown in Figure 2.5.

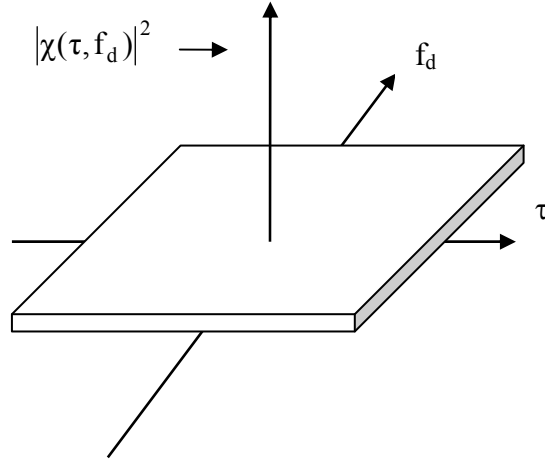


Figure 2.5: Ideal ambiguity diagram.

The chaotic signal can be seen as a stochastic process if the initial conditions are changed randomly. The ensemble average of the ambiguity function can be obtained using equation 2.51, which is the discrete version of the ambiguity function where M is the number of realizations.

$$E\{\chi(m, \omega)\} = \frac{1}{M} \sum_{m=-l}^M \sum_{n=1}^N [s(n) \cdot s(n+m) \cdot e^{-j2\pi\omega n}] \quad (2.51)$$

2.7.3 Range Information

At the receiver, signal processing is done to extract the information of the target as it is the range and Doppler information. The range of the target R can be computed by measuring the time that takes to the signal to go out from the transmitter reflect from the target, and return back to the receiver. The range is calculated using equation 2.52 [32]:

$$R = \frac{c\tau}{2} \quad (2.52)$$

where c is the speed of light and τ is the time delay.

The range resolution is a measure that can be used to describe the ability of the LADAR to distinguish between two targets in the range plane. The range resolution depends on the transmitted signal and can be calculated using equation 2.53 [32]:

$$\Delta R = \frac{c}{2\beta_c} \quad (2.53)$$

where c is the speed of light and β_c is the compression bandwidth of the signal.

The bandwidth of the transmitted signal can be measured by using the autocorrelation. The width of the main lobe of the autocorrelation is inversely proportional to the effective bandwidth of the signal. When the power spectrum has significant fluctuations over the band of interest, as in the case of a chaotic signal, the bandwidth is calculated using a root mean square approach:

$$\beta_e = \sqrt{\frac{\sum f_i^2 X(f_i)}{\sum X(f_i)} - \left[\frac{\sum f_i X(f_i)}{\sum X(f_i)} \right]^2} \quad (2.54)$$

where $\mathbf{f} = [f_1 \ f_2 \ \dots \ f_N]$ is a vector of the frequency components in the power spectrum, $\mathbf{X}(\mathbf{f}) = [X_1 \ X_2 \ \dots \ X_N]$ is the vector with the values of the power spectrum. It should be emphasized that β_c and β_e are not necessarily the same.

2.7.4 Doppler Information

The Doppler resolution is defined as the ability of radar to separate between two spaced objects. In other words is the ability of LADAR to resolve the target radial velocity. In order to define the Doppler resolution, the Doppler shift has to be defined first. The Doppler shift that is produced by a single point with a radial velocity v is defined as [30]:

$$f_d = \frac{2v}{\lambda} \quad (2.55)$$

where λ is the wavelength, c is the speed of light, v is the velocity of the target. The Doppler resolution can be calculated by using the following equation:

$$\Delta f_d = \frac{1}{T_1} \quad (2.56)$$

where T_1 is the pulse width or duration of the signal.

Chapter 3: Characterization of Chaotic Signal

3.1 Time Domain and Pseudo Phase Maps

Chaotic time series have an apparent random behavior with no visible periodicity in the time domain. Although much more evidence than the time behavior is needed to confirm that a series is chaotic, time domain plots are a good method for inspecting the behavior of the series.

For simulation purposes, the Lang-Kobayashi equations are solved by using a fourth order Runge-Kutta numerical integrator. The feedback level k is easily adjusted to verify the behavior of the electric field in the periodic, mode hopping, and chaotic regimes of the system. For simplicity, the results are described in terms of the normalized parameters of the of the Lang-Kobayashi equations. Of course, the same results can be obtained with equations 2.9-2.11.

After eliminating the samples corresponding to the transit time of the external cavity, a time series 0.8ns in length is obtained. As expected, in the absence of any feedback, simulations show that the complex envelope of the field is constant. Next, the feedback level is set to $\eta=0.001$. The resulting

periodic field of the laser output is observed in Figure 3.1. The electric field has a periodic behavior and is shaped by a single harmonic. The period of the periodic signal depends on the feedback level. The period is inversely proportional to the feedback level and as the feedback level increases the period of the signal decreases. However, the period is also directly proportional to the frequency of oscillation, so as the feedback level increases, the oscillation frequency increases. The frequency of oscillation can be determined by using the power spectrum of the signal.

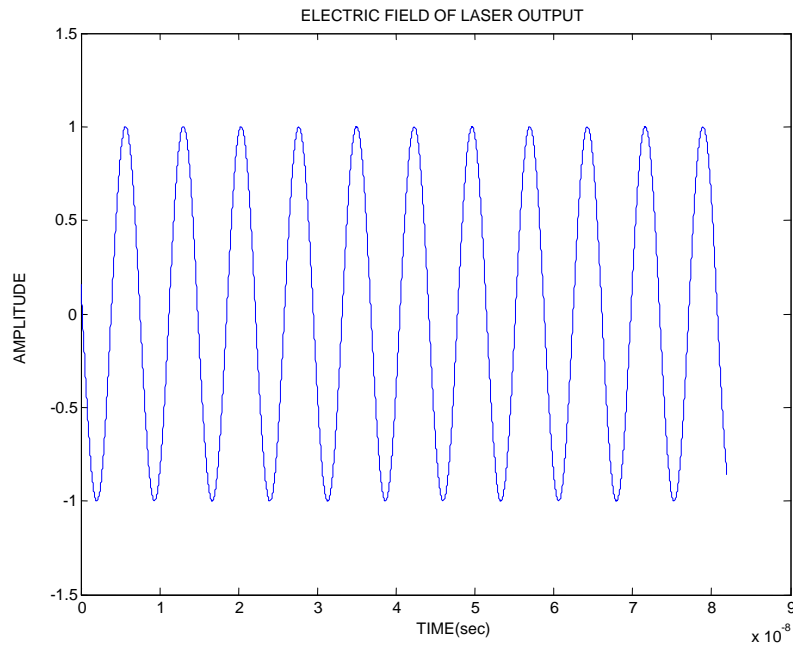


Figure 3.1: Time behavior of periodic electric field.

The intensity of the laser output is obtained by computing the magnitude square of the electric field. The intensity of the laser output for a feedback level in the periodic regime is shown in Figure 3.2. Notice that the frequency is twice that of the electric field.

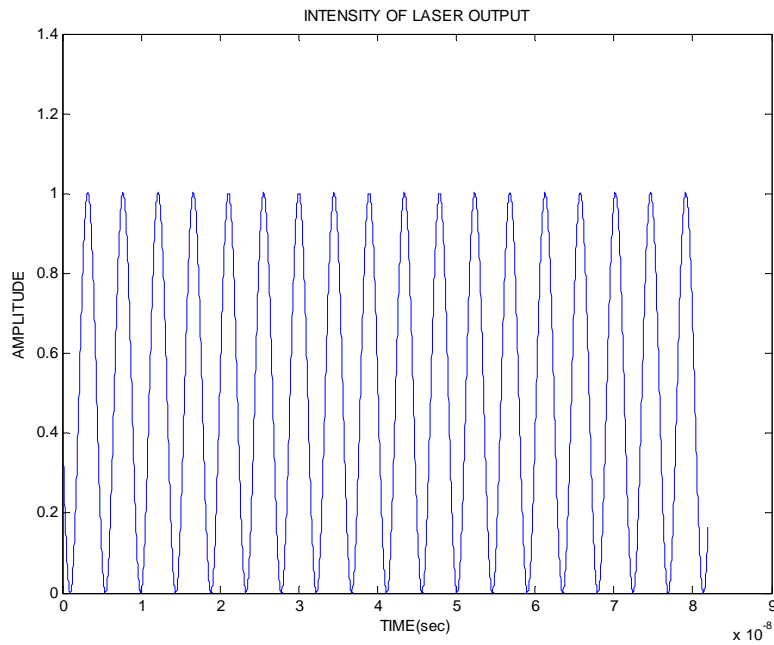


Figure 3.2: Time behavior of intensity of laser output in the periodic regime.

By increasing the feedback level, the signal is forced into the mode hopping regime and is no longer monotone. Instead, several frequency components should appear. The time domain plot of the output of the laser for $\eta=0.01$ is shown in Figure 3.3 with a shape determined by the amplitude and phase of the multiple components. A close up of the intensity of the laser output in the mode hopping regime is illustrated in Figure 3.4 showing that the signal is still periodic.

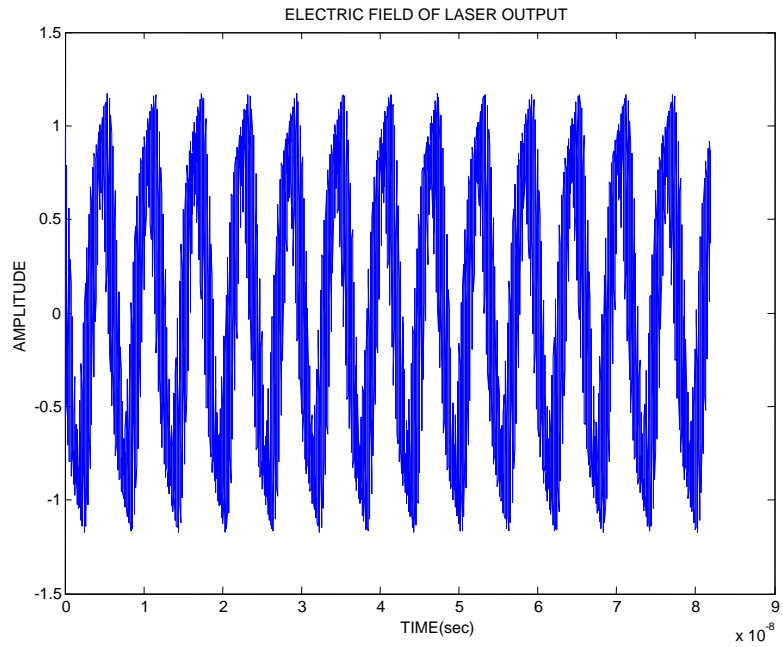


Figure 3.3: Time behavior of mode hopping electric field.

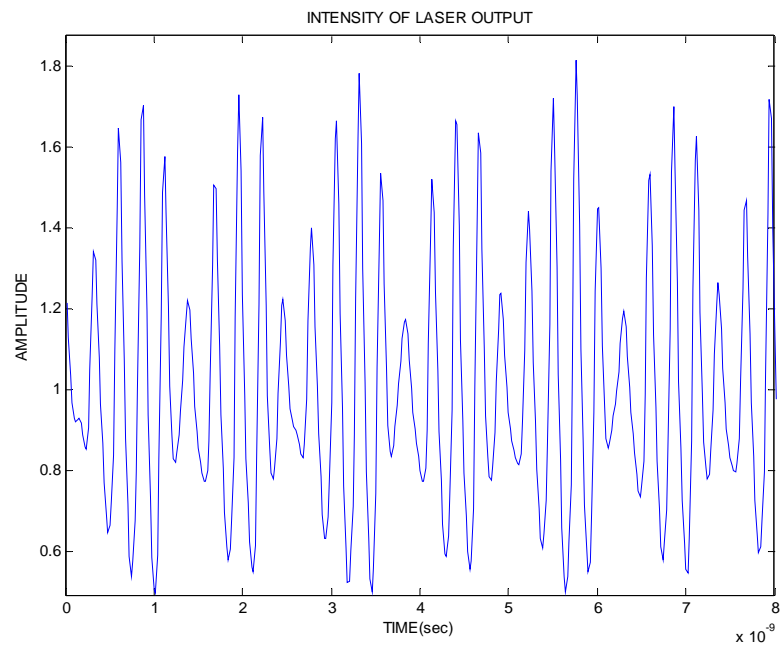


Figure 3.4: Time behavior of intensity of laser output in the mode hopping regime.

As the feedback level is increased to 0.06, the electric field in the time domain becomes chaotic. The time domain behavior is shown in Figure 3.5. Here, the signal has an apparent random behavior in

time. A detailed analysis of the frequency components of the signal will be provided in the following section.

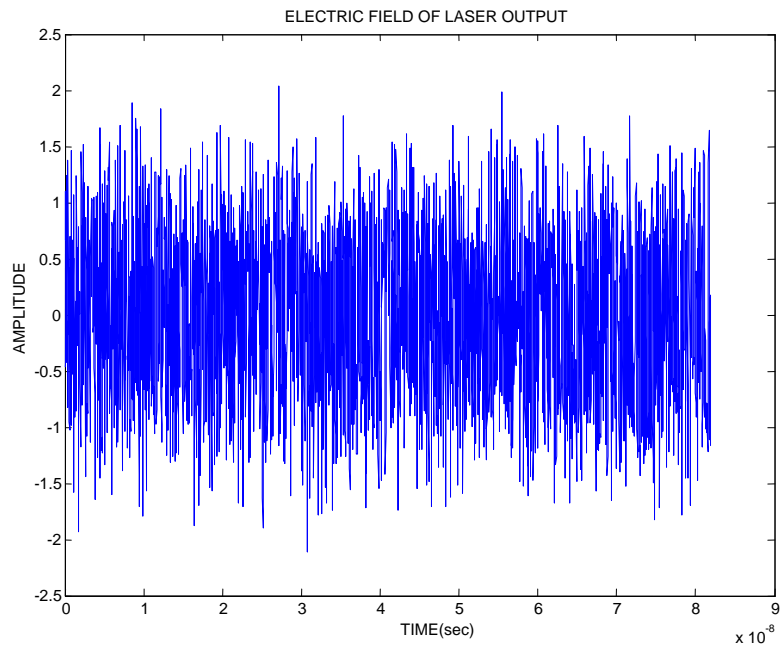


Figure 3.5: Time behavior of chaotic electric field.

The intensity of the laser output for a feedback level in the chaotic regime is shown in Figure 3.6. In this case, it is evident that the output is composed of random fluctuations.

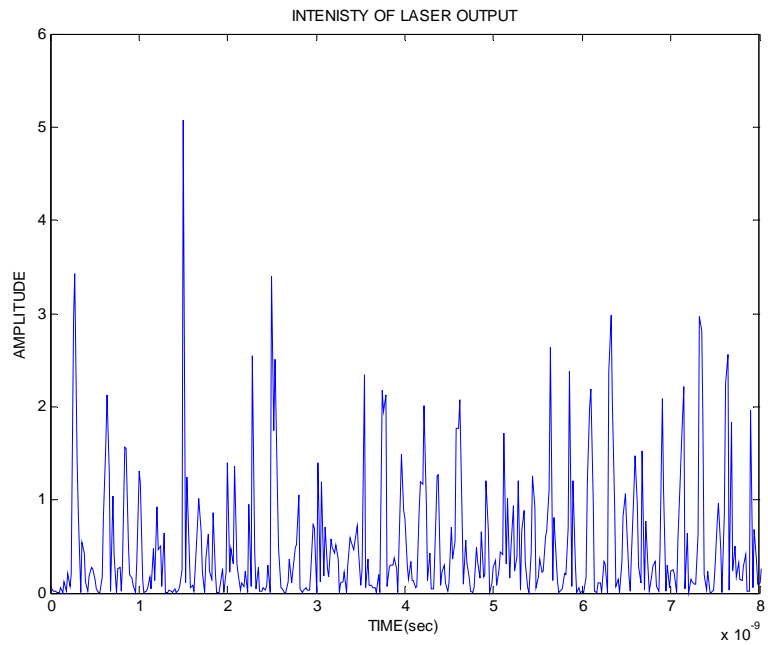


Figure 3.6: Time behavior of intensity of laser output in the chaotic regime.

For completeness purposes, it is important to make sure that the carrier density and the phase of the dynamic system are not periodic. Figure 3.7 shows the time behavior of the carrier density which has an apparent random behavior in time with no periodic component.

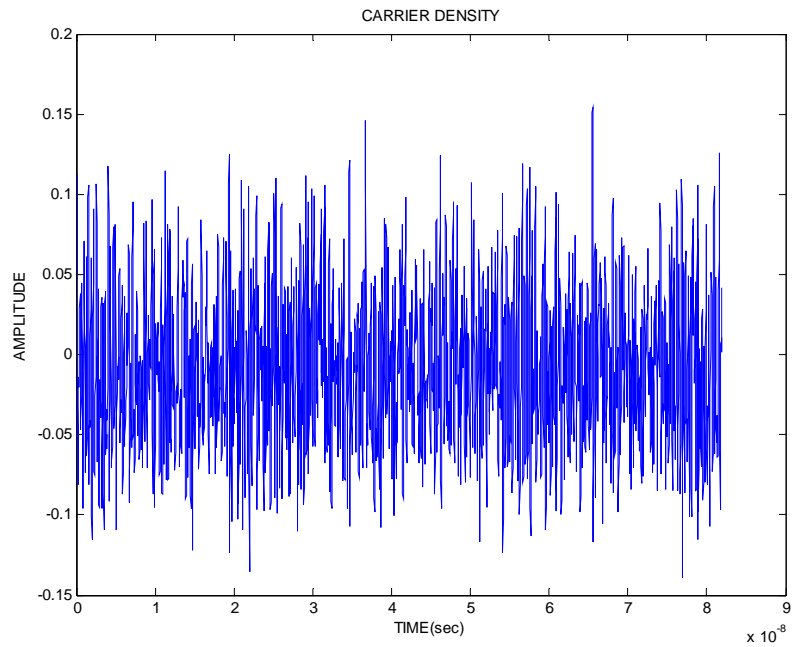


Figure 3.7: Time behavior of carrier density in chaotic regime.

Figure 3.8 shows the time behavior of the phase of the electromagnetic field. The phase is smooth but does present a chaotic behavior. The discontinuities in phase are due to fold over and can be easily unwrapped.

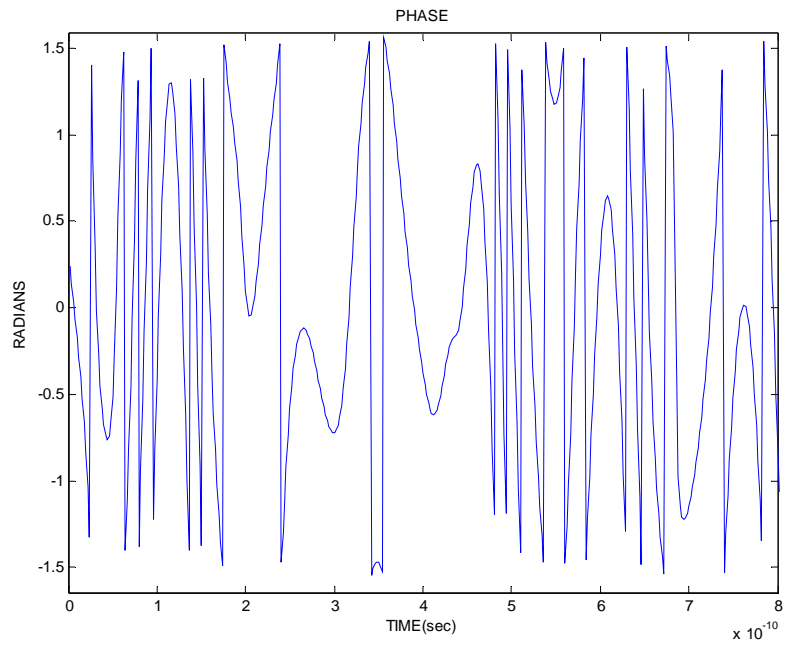


Figure 3.8: Time behavior of phase in chaotic regime.

It is worth mentioning that the examples above illustrate the evolution of the electric field and the intensity of the laser output, but neither their chaotic behavior nor their fractal nature have been demonstrated. Although the coherence of the system has collapsed, the fundamental question of whether the field is chaotic or not has yet to be answered. This requires an analysis of the state space orbit.

In a multi-dimensional system such as the Lang-Kobayashi set of equations, the chaotic performance can be directly inferred by plotting the three state variables in a 3-D space and observing the orbit of the system as it evolves into a strange attractor as will be described in the next section. Alternatively, diffeomorphism can be used when data from only one of the state variables is available [27]. In this instance, a version of the attractor can be constructed by considering delayed versions of the state variable. For instance, since the electric field is the only observable variable, its attractor can be generated by looking at $E(t)$ vs. $E'(t)$ or $E(n)$ vs. $E(n+1)$.

The plot of $E(n)$ versus $E(n+1)$ is commonly referred to as a pseudo-phase diagram. The relationship between samples can be distinguished by using this plot. For a better understanding of pseudo phase maps and for comparison the pseudo phase map of a random signal, a periodic signal and a chaotic signal are shown. For comparison purposes, the pseudo phase map of a random signal was generated using a uniform random generator. The pseudo phase map of the electric field of the laser was obtained for $\eta=0.001$ and for $\eta=0.06$. In the case of the random field, the pseudo phase map is composed of many points that are distributed uniformly and do not have any trajectory or relationship as shown in Figure 3.9. For the periodic field, the pseudo phase map has only one orbit reminiscent of the Lissajou pattern commonly used to characterize oscillating electronic circuits. The resulting plot is shown in Figure 3.10. In contrast, the pseudo phase map of the chaotic signal has several orbits and a complex non repeated behavior is shown in Figure 3.11. Figure 3.12 shows a zoom in of the attractor of the chaotic signal. Since the orbit forms a strange attractor this establishes that the electric field of the laser output for $\eta=0.06$ has a chaotic behavior.

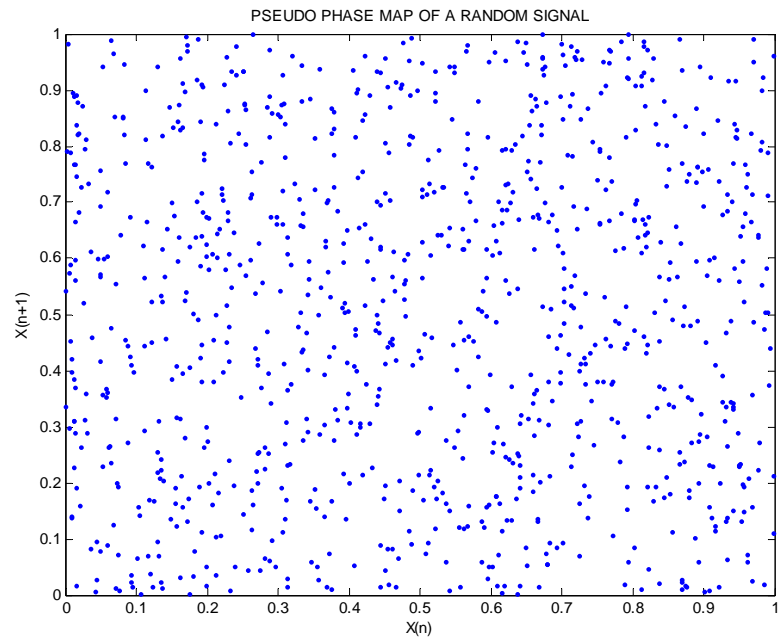


Figure 3.9: Pseudo phase map of a random field.

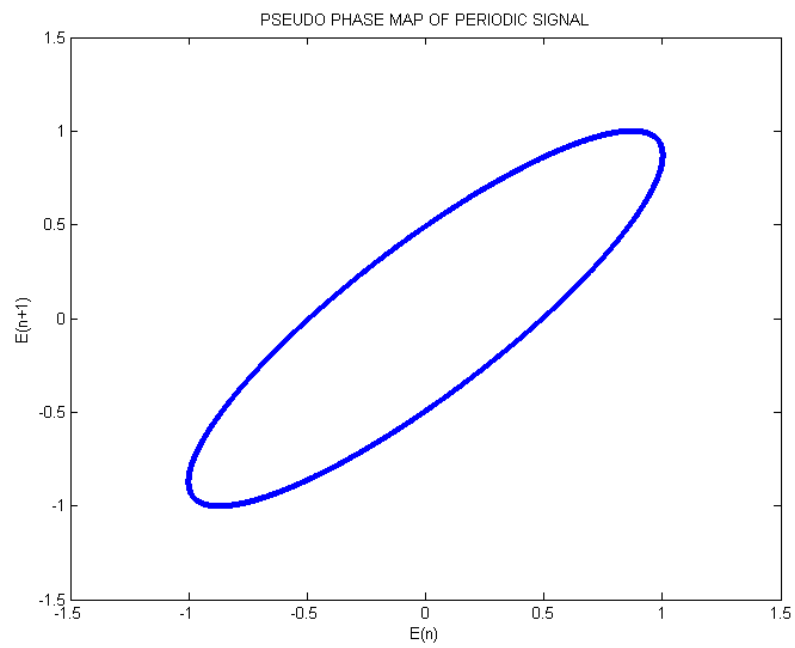


Figure 3.10: Pseudo phase map of periodic field.

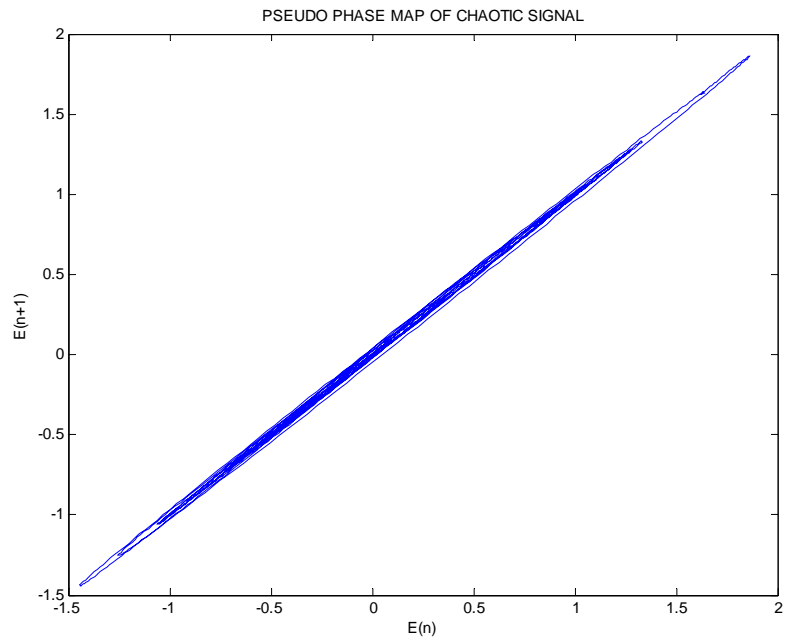


Figure 3.11: Pseudo phase diagram of chaotic field.

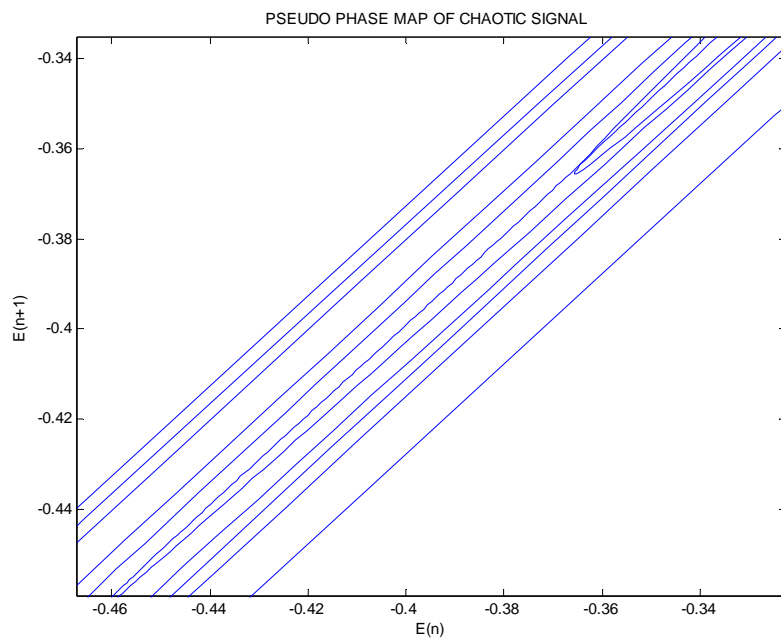


Figure 3.12: Zoom in of the phase map of the chaotic field.

The pseudo phase maps of the carrier density and the phase are shown in Figure 3.13 and Figure 3.14 respectively. In Figure 3.13, it can be observed that there is relationship between the current and

next sample of the carrier density. The pseudo phase map has a complex behavior that consists of several orbits that do not repeat. This clearly illustrates that there is a relationship between samples that is confined to a strange attractor. In both cases the pseudo phase maps are those of a chaotic signal.

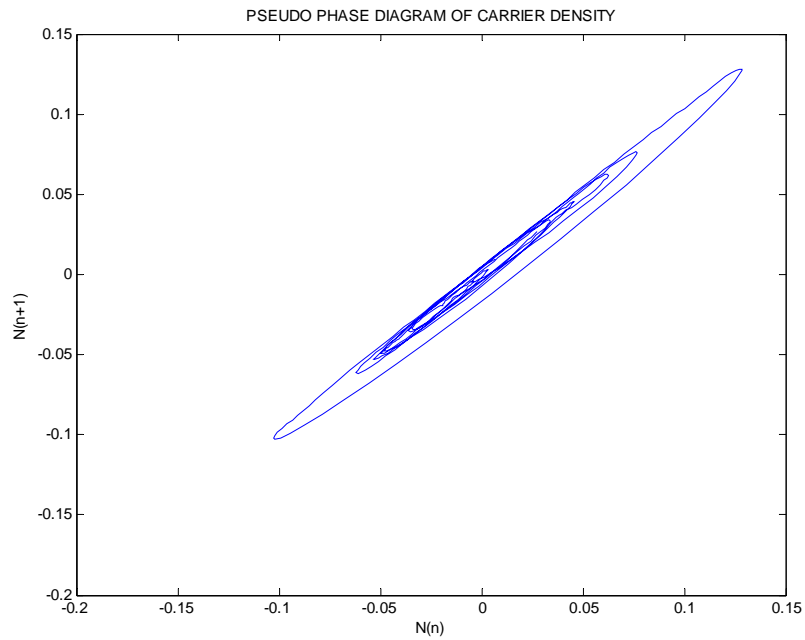


Figure 3.13: Pseudo phase map of carrier density in chaotic regime.

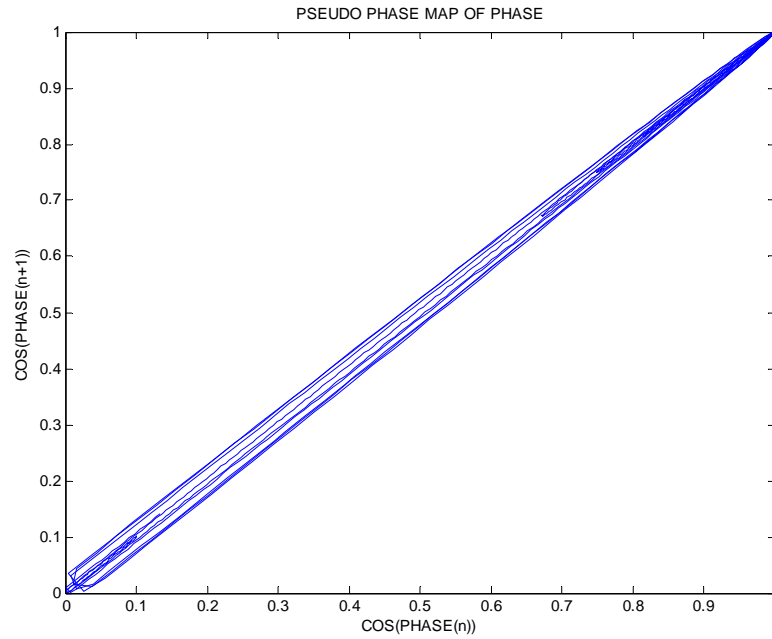


Figure 3.14: Pseudo phase map of phase.

3.2 Attractor of the System and Lyapunov Exponent

The attractor defines the behavior of the system variables. Specifically, for a semiconductor laser with feedback the attractor is a three dimensional plot of the carrier density, the electric field of the laser output, and its phase. In Figure 3.15 the attractor of the system for $\eta=0.001$ can be observed. In this case, the attractor of the system consists of just one orbit (or limit cycle) because the orbit follows a periodic pattern.

ATTRACTOR OF PERIODIC SIGNAL

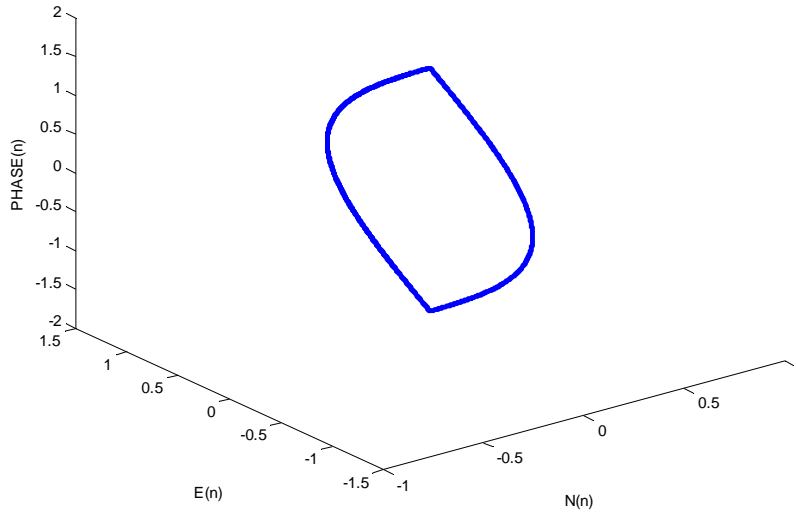


Figure 3.15: Attractor of the system in the periodic regime.

As the feedback level is increased to 0.01 the signal enters into a quasi-periodic regime or mode hopping regime. In this case the attractor of the system follows what is called a torus form. The attractor of the system in the mode hopping region is shown in Figure 3.16.

ATTRACTOR OF QUASIPERIODIC SIGNAL

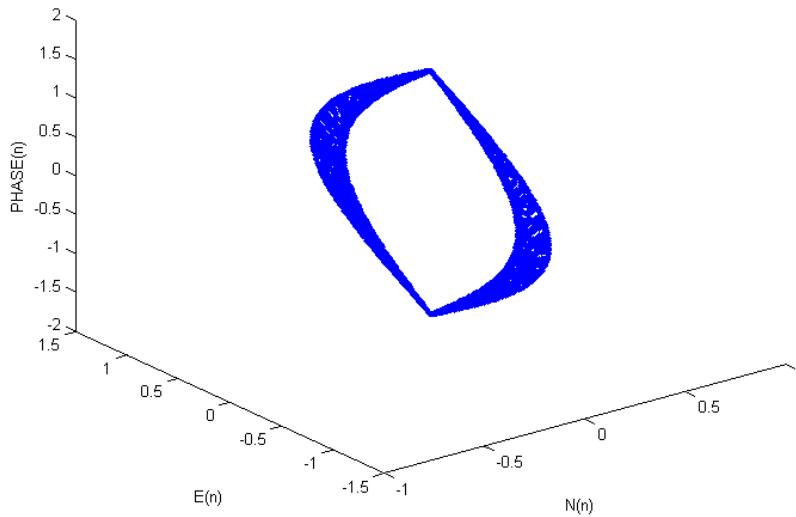


Figure 3.16: Attractor of the system in the mode hopping region.

For $\eta=0.06$ the system becomes chaotic as shown in Figure 3.17. In this case, the attractor follows a complex but deterministic trajectory.

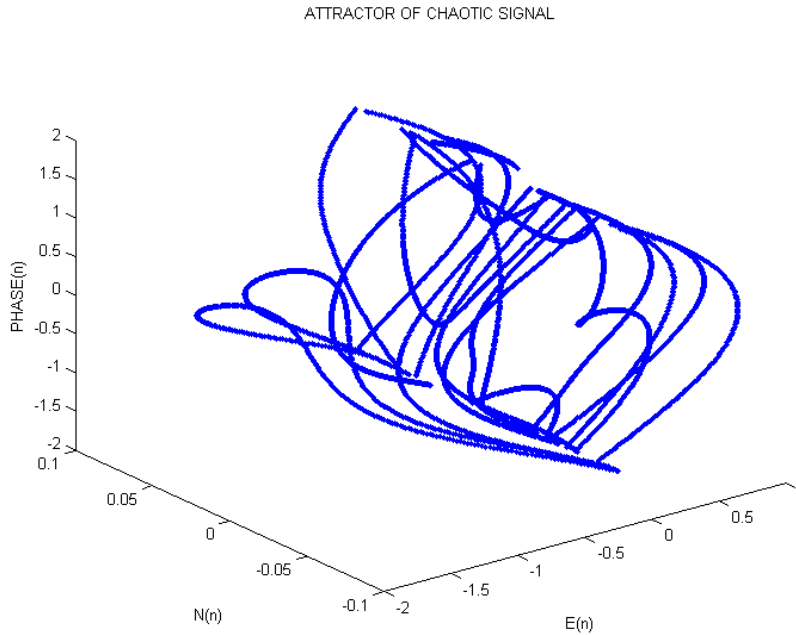


Figure 3.17: Attractor of system in the chaotic regime.

The largest Lyapunov exponent was calculated for the four regimes of the laser output by using the numerical approach defined in chapter 2. Table 3.1 shows the Lyapunov exponent calculation for each regime. In the chaotic regime the Lyapunov exponent is greater than in the other three regimes. As anticipated, in the periodic regime, the Lyapunov exponent is close to zero.

Table 3.1: Lyapunov exponents for different regimes

Regime	κ	η	λ_1
Periodic	0.0008	0.001	0.0395
Mode Hopping	0.008	0.01	0.1131
Chaotic	0.052	0.06	0.3208
Periodic	0.433	0.5	0.0127

3.3 Time Series Properties

In previous sections the Lang-Kobayashi equations were solved by setting the initial conditions to fixed values. The control parameters in this case can be modified so the desired signal is obtained. However, when a LADAR receiver captures a signal that is returning back from a target, the original conditions are not necessarily known by the receiver. In this case, the receiver only captures the experimental data or the time series data. Therefore, it is important to analyze the time series properties and discover if the statistical properties change with time. In the case that the statistical properties are the same, whether they are calculated from a probabilistic approach or via a temporal time analysis, the system is said to be ergodic.

In order to perform the temporal time analysis, a total of 100,000 samples of the electric field are used. In this case, the laser output is set in the chaotic regime by setting the feedback level at 0.06 and the external cavity length to 0.09m. To perform the equivalent probabilistic analysis the experiment is run 1000 times. Each time the initial conditions of the Lang-Kobayashi equations are changed. The electric field of the 10,000th sample in each run is saved.

Next, the first four moments are calculated for the temporal and ensemble electric field vectors. The mean of the time series vector was calculated by computing its average as follows:

$$\langle X \rangle = \frac{1}{N} \sum_{n=1}^N X_n \quad (3.1)$$

The standard deviation which is the width of the distribution was calculated as:

$$\sigma = \sqrt{\frac{1}{N-1} \sum_{n=1}^N (X_n - \langle X \rangle)^2} \quad (3.2)$$

The symmetry or skewness of the distribution can be measured by using the third moment given by

$$s = \frac{1}{N} \sum_{n=1}^N \left[\frac{X_n - \langle X \rangle}{\sigma} \right]^3 \quad (3.3)$$

If the skewness is positive the distribution mass is concentrated to the right of the mean. In the case that the skewness is negative the distribution mass is concentrated to the left of the mean. If the skewness results to be zero that means that the distribution is symmetric about the mean. The kurtosis is defined as the fourth moment. The kurtosis is used to measure the peakedness of the distribution compared to a Gaussian distribution. The kurtosis can be calculated as:

$$k = \frac{1}{N} \sum_{n=1}^N \left[\frac{X_n - \langle X \rangle}{\sigma} \right]^4 - 3 \quad (3.4)$$

The kurtosis for a Gaussian distribution is zero. Therefore, if a kurtosis is positive the distribution is called leptokurtic or flat tailed; if the kurtosis is negative the distribution is called platykurtic.

To test the ergodicity of the field, a vector consisting of 100,000 iterations is created. The four moments are calculated for this time series. Results are shown in Table 3.2. The mean of the electric field is almost zero, the standard deviation is close to 1, the mass is concentrated on the left side based on the skewness, and the distribution is platykurtic based on the kurtosis.

Table 3.2: Probabilistic and temporal statistical properties of electric field

Parameter	Probabilistic	Temporal
Mean	0.005	0.002
Standard Deviation	0.7112	0.719
Skewness	-0.027	-0.016
Kurtosis	-0.6123	-0.588

The probability distribution of the amplitude of the electric field is shown in Figure 3.18. The probability distribution has a quasi-Gaussian shape.

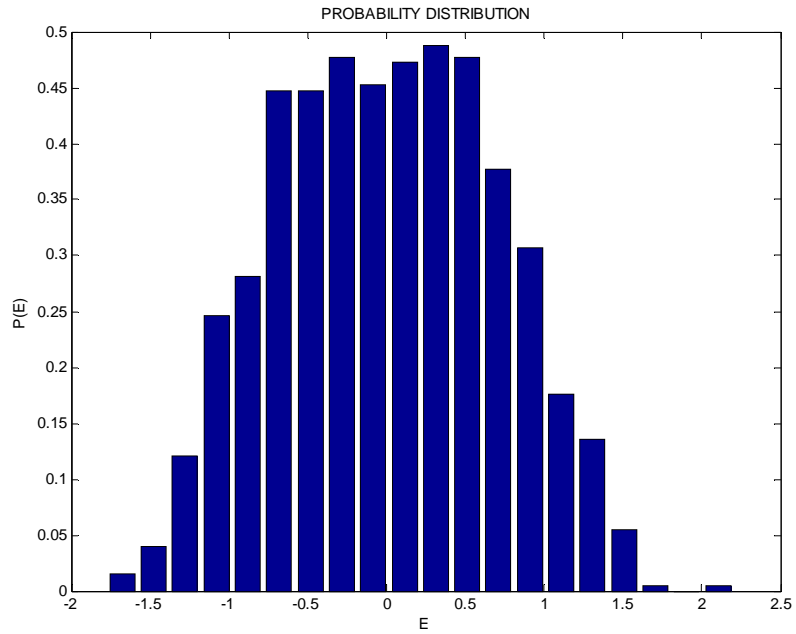


Figure 3.18: Probability density of electric field based on one realization.

The probability density function of the 10,000th sample of the electric field is shown in Figure 3.19.

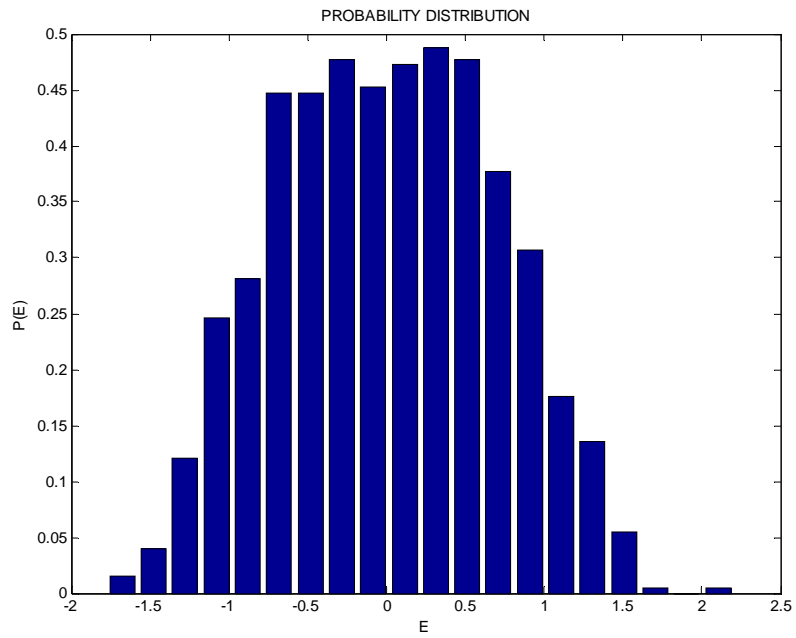


Figure 3.19: Probability density of n^{th} sample of the electric field.

The corresponding estimates of the four moments are very close to each other. Furthermore, the probability distributions are similar. Hence, the electric field can be assumed to be ergodic.

3.4 Power Spectrum and Autocorrelation

To analyze the impact that the control parameters have on the power spectrum of the electric field, the bifurcation diagram of the power spectrum is obtained. Figure 3.20 shows the bifurcation diagram of the power spectrum for a fixed external cavity length and varying the feedback level. For each feedback level the power spectrum of the electric signal is obtained and plotted versus the frequency. For illustration purposes, the power spectrum was normalized to its maximum value. The power spectrum of the electric field has a dependence on the feedback level. As the feedback level increases, more frequencies appear on the power spectrum. At low feedback level, the power spectrum is composed of just one frequency. As the feedback level is increased more frequency components appear on the power spectrum until chaos is reached where many frequency components are present.

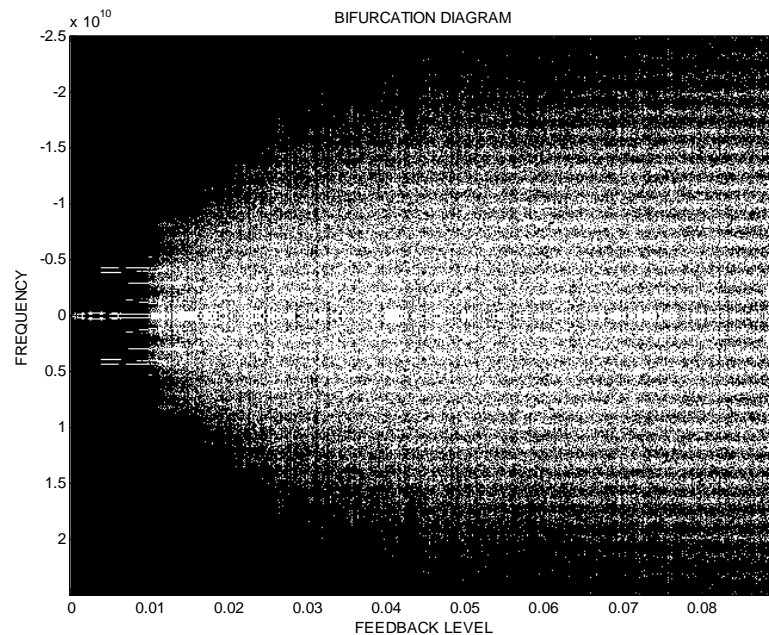


Figure 3.20: Bifurcation diagram for a fixed external cavity length.

In addition, the influence that the external cavity length has on the power spectrum was analyzed by maintaining the feedback level fixed and varying the external cavity length. Figure 3.21 shows the

bifurcation diagram of the power spectrum varying the external cavity length from $0.00001\text{m} < L_{\text{ext}} < 0.30\text{m}$. It can be observed that the power spectrum of the electric field does not go to another regime as the external cavity length is changed. The power spectrum of the signal is periodic.

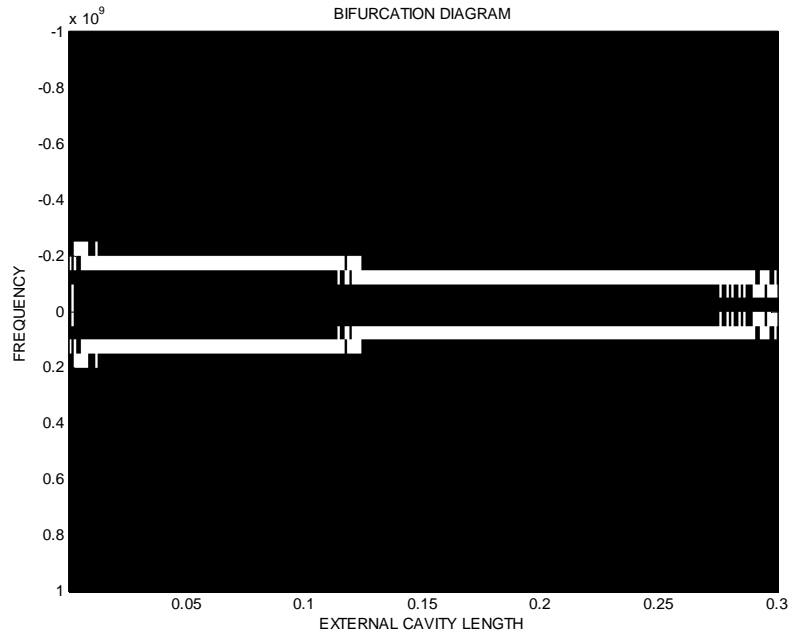


Figure 3.21: Bifurcation diagram for a fixed feedback level.

The power spectrum of the electric field is calculated using equation 2.31. After, eliminating the transient samples, a total of 4096 samples are used. An average of 10 power spectra is obtained to have a more accurate result. The power spectrum of the electric field for the periodic regime is shown in Figure 3.22. In this case, the power spectrum has one frequency component. This means that the signal is periodic. The same power spectrum is obtained by setting the feedback level in the range of $0 < k < 0.01$. In that feedback level regime, just one frequency is present. However, the frequency is dependent on the feedback level. As the feedback level increases, the frequency of the periodic signal increases.

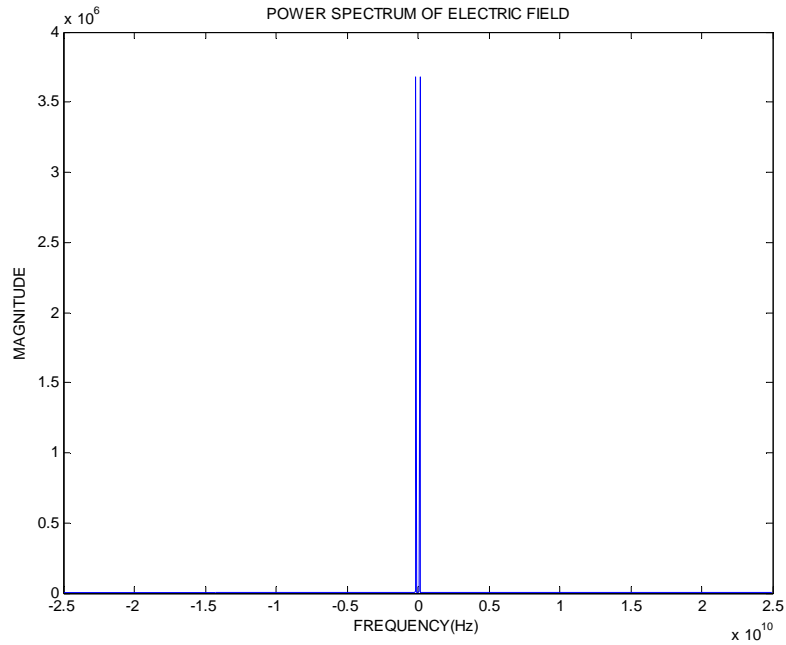


Figure 3.22: Power spectrum of the electric field for the periodic regime.

Figure 3.23, shows the power spectrum of the laser output for $\eta=0.01$. Many frequencies become apparent. The separation between the frequencies is inversely proportional to the external cavity length as

$$f_{\text{ext}} = \frac{c}{2L_{\text{ext}}} = \frac{3 \times 10^8}{2(0.09)} = 0.166 \times 10^{10} \text{ Hz} \quad (3.5)$$

The frequencies on the power spectrum can be easily distinguished as multiples of the external frequency f_{ext} . This type of behavior is encountered for a feedback level around $0.001 < k < 0.019$.

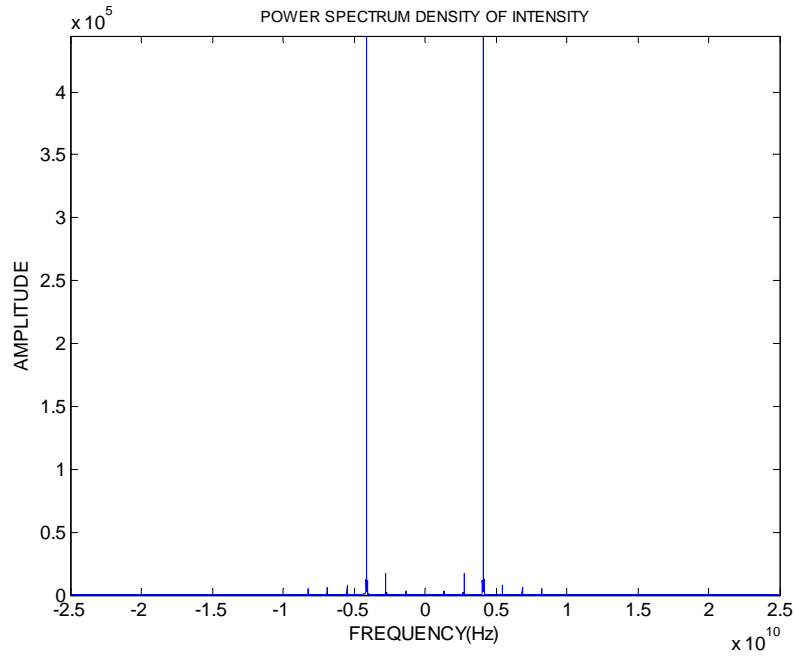


Figure 3.23: Power spectrum of the electric field for the mode hopping regime.

Figure 3.24 shows the power spectral density of the laser output for $\eta=0.06$. There are frequency components in this case, and the bandwidth increases up to 22GHz. The external cavity frequency cannot be distinguished anymore. In this case, the coherence of the laser collapses and the amplitude of the power spectrum is significantly lower than the amplitude of the power spectrum in the periodic regime. In fact, the amplitude of the power spectrum in the chaotic regime is 100 times lower than the one of the periodic regime. These type of behavior of the power spectrum is encountered for a feedback level $0.01 < k < 0.10$.

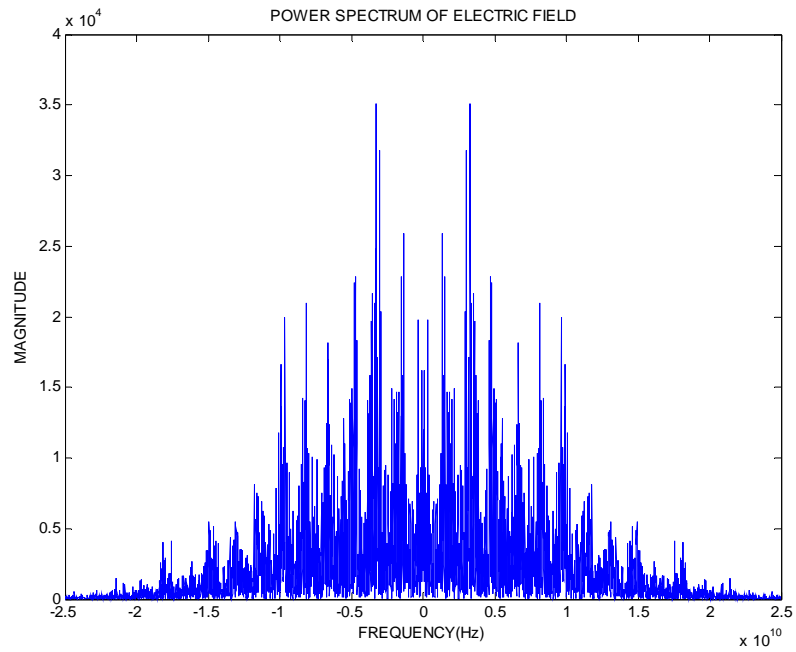


Figure 3.24: Power spectrum of the electric field for the chaotic regime.

The autocorrelation of the electric field is calculated using equation 2.33. The autocorrelation of the electric field for $\eta=0.001$ is shown in Figure 3.25. In this case, the autocorrelation has many sidelobes. As the time lag is varied, the sidelobes of the autocorrelation do not decrease significantly. That is an indication that that the signal is not chaotic or random it is periodic.

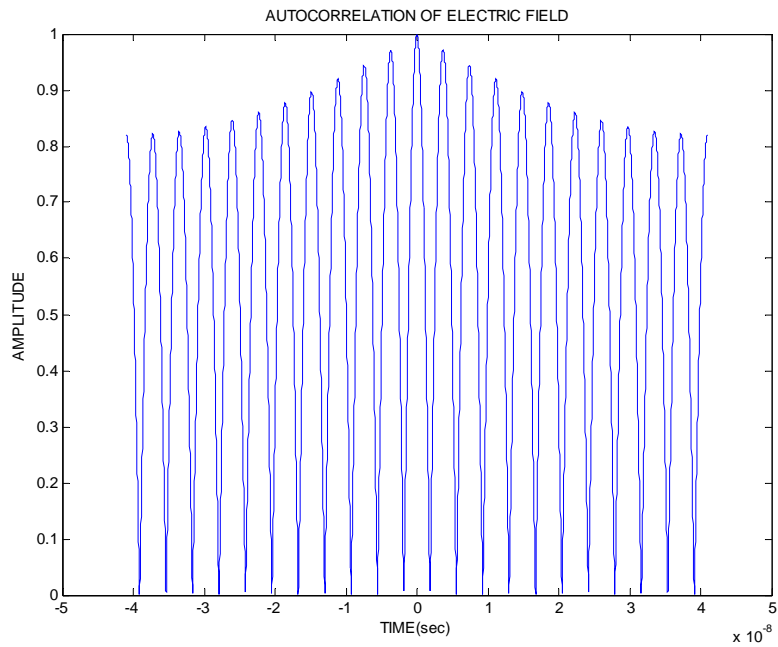


Figure 3.25: Autocorrelation of the electric field for the periodic regime.

The autocorrelation of the electric field for a feedback level $\eta=0.01$ is shown in Figure 3.26. In this case, the same pattern is repeated. This is an indication that the electric field signal has some periodic behavior. The autocorrelation of the signal has a triangular envelope, but the side lobe levels are quite high.

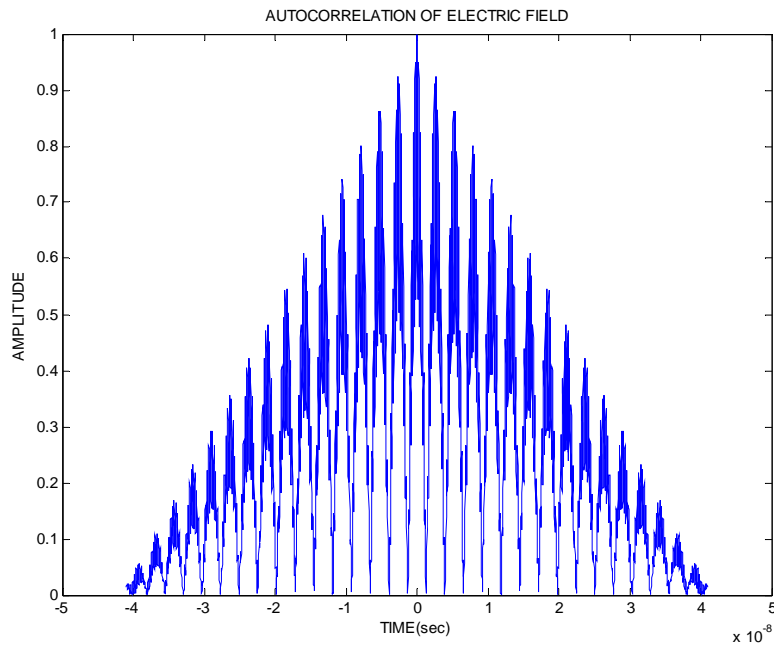


Figure 3.26: Autocorrelation of the electric field for the mode hopping regime.

The autocorrelation of the electric field for a feedback level $\eta=0.06$ is shown in Figure 3.27. In this case the autocorrelation has one peak and the signal decorrelates with time. The autocorrelation does not repeat itself, which is an indication that no periodic component is present. The side lobes are less than 0.3. A detail analysis of the field in the chaotic regime will be performed in next section.

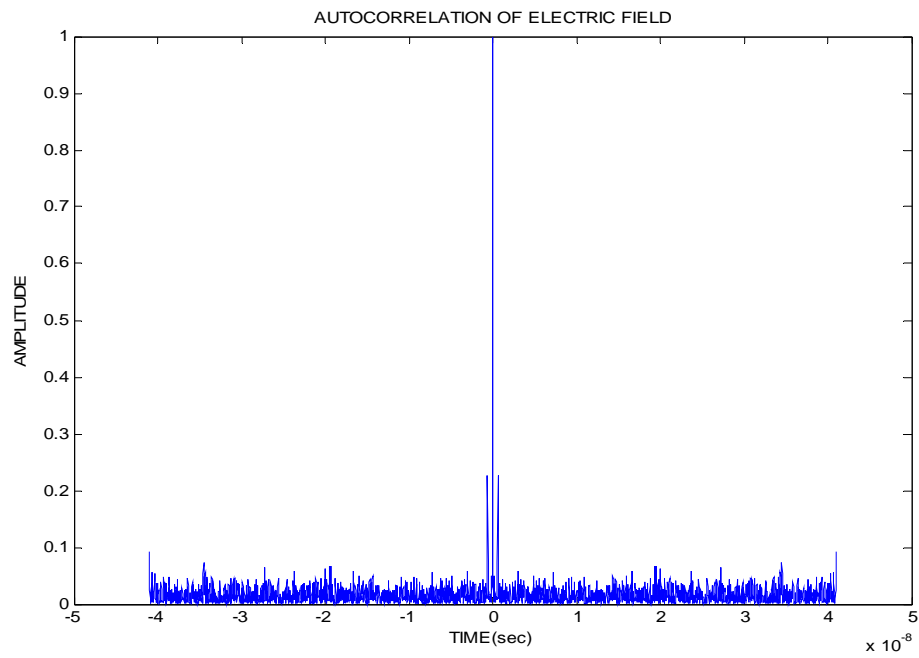


Figure 3.27: Autocorrelation of the electric field for the chaotic regime.

Chapter 4: Optimization of Control Parameters

4.1 Parameter Selection Approach

In ranging applications, the selection of the transmitted signal is a crucial matter since it becomes the reference against which the echo from the target is compared. More specifically, in the detection process, the echo is correlated with the transmitted signal to obtain the distribution of the scattering point of the target in the range-Doppler domain. In this plane, the bandwidth of the transmitted signal determines the range resolution while its duration determines the Doppler resolution.

There is, of course, a myriad of signals that could be used depending on the target or scenario to be mapped. A signal that has optimal properties can be deterministic, chaotic, or random. Properties for deterministic and random signals have been studied extensively. Those of a chaotic signal are less well known. For this reason, we propose that an ideal chaotic signal must have the following properties:

- Ergodicity
- Flat, wide spectrum
- Narrow autocorrelation
- Negligible autocorrelation and ambiguity surface sidelobes
- Low ambiguity surface entropy
- High Lyapunov exponent

In what follows we consider the chaotic signal obtained with the optical feedback semiconductor laser described above. It is important to mention that the optimization of the signal is performed in the chaotic regime of the laser output. The other two regimes are not considered.

4.2 Statistical Properties of Chaotic Signal

Although the chaotic signal is strictly deterministic, it can be treated as the realization of a random process provided that the initial conditions of the laser dynamical system are unknown. In this

case, the statistical properties of the chaotic signal become of interest. To start, the first four moments of the chaotic signal are obtained.

Consider 100,000 samples of the chaotic signal generated by setting the feedback level to 0.05. For this experiment, the feedback level is fixed to 0.05 and the external cavity length is varied initially in steps of 0.01 m and then in steps of 0.05m. Similar tests were performed by using the length of the external cavity as a multiple of the laser’s original half wavelength. Table 4.1 shows the corresponding statistical properties of the probability density function of the chaotic signal. Changing the external cavity length does not appear to have a significant impact on the standard deviation of the chaotic signal. However, the mean, the kurtosis and the skewness does vary somewhat but not in a discernible pattern.

Table 4.1: Four moments of the chaotic signal for variable external cavity length

Cavity Length (m)	Mean	Standard Deviation	Skewness	Kurtosis
0.05	-0.019	0.717	0.032	-0.624
0.10	-0.019	0.721	0.036	-0.549
0.15	-0.003	0.716	0.028	-0.542
0.20	-0.003	0.719	0.030	-0.485
0.25	-0.023	0.721	0.004	-0.579
0.30	-0.002	0.718	0.003	-0.545

The next step is to analyze the influence that the feedback level has on the statistical properties of the chaotic signal. For this experiment, 100,000 samples of the chaotic signal were generated by setting the external cavity length to $L_{ext}= 0.30\text{m}$ while varying the feedback level between 2 percent and 9 percent in increments of 1 percent. As shown in Table 4.2, the feedback level that provides a signal with a mean close to zero is 0.05. In this case, the probability distribution is almost symmetric about the origin having a skewness of 0.003. However, the distribution is not Gaussian since the kurtosis deviates significantly from 3.0.

Table 4.2: Four sample moments of chaotic signal for various feedback levels

Feedback level	Mean	Standard Deviation	Skewness	Kurtosis
0.02	0.056	0.697	-0.067	-1.055
0.03	-0.003	0.715	-0.025	-0.894
0.04	-0.007	0.720	-0.035	-0.594
0.05	-0.002	0.718	0.003	-0.545
0.06	-0.013	0.720	0.027	-0.567
0.07	-0.044	0.725	0.040	-0.528
0.08	-0.020	0.737	0.015	-0.437
0.09	-0.015	0.737	-0.023	-0.418

4.3 Autocorrelation and Power Spectrum for Variable External Cavity Length

For the analysis of the autocorrelation and power spectrum of signal, a total of N iterations of the Lang – Kobayashi equations are computed. In practice, the first m samples should be discarded to allow the state variables to settle into the strange attractor. Therefore, a total of N-m samples are used to study the chaotic signal. To reduce the fluctuations in the autocorrelation and the power spectrum, M runs of the experiment should be conducted to obtain ensemble averages. In what follows, N =6096, m=2000, and N-m=4096. This last value is chosen so that the fast Fourier transform computations are done efficiently.

In this case the Lang-Kobayashi equations are solved by setting the feedback level η to 0.05 (5 percent). This value of feedback level is in the chaotic regime. Next, the external cavity length is set to 0.05 m. The autocorrelation of the electric field is shown in Figure 4.1. In this case, the major side lobe level is 0.2132. The major sidelobe level is located at a time equal to the external round trip time given by

$$\tau_{\text{ext}} = \frac{2L_{\text{ext}}}{c} = \frac{2(0.05)}{3 \times 10^8} = 0.33 \times 10^{-9} \text{ sec.} \quad (4.1)$$

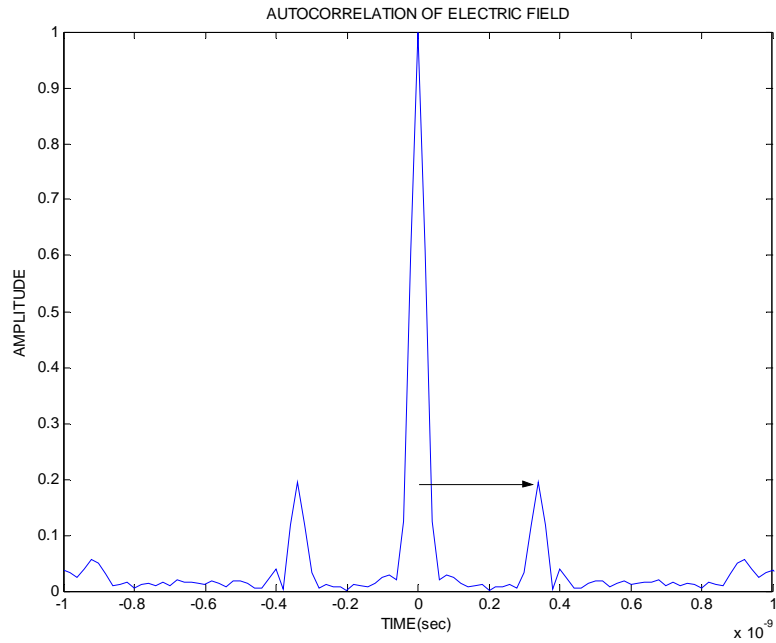


Figure 4.1: Autocorrelation of the electric field for $L_{\text{ext}}=0.05$ m.

The autocorrelation of the electric field was obtained for an external cavity length of 0.15 m and is shown in Figure 4.2. In this case the major sidelobe is 0.2332, which is relatively high, and is located at a time equal to the external cavity round trip $\tau_{\text{ext}}=0.866 \times 10^{-9}$ sec.

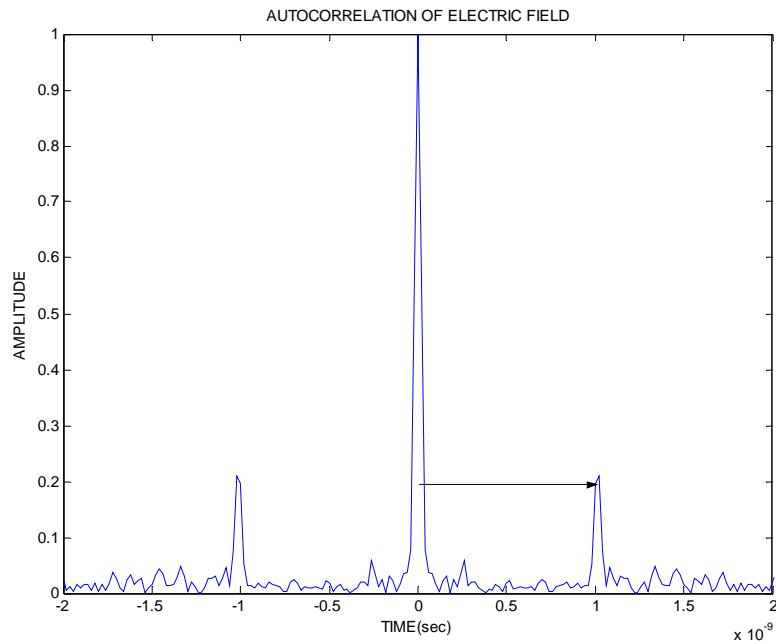


Figure 4.2: Autocorrelation of the electric field for $L_{\text{ext}}=0.15$ m.

The autocorrelation of the electric field for an external cavity length of 0.30m is shown in Figure 4.3. In this case, the major sidelobe level has a maximum value of 0.1996 and the major sidelobe is located at $\tau_{\text{ext}}=2 \times 10^{-9}$ sec.

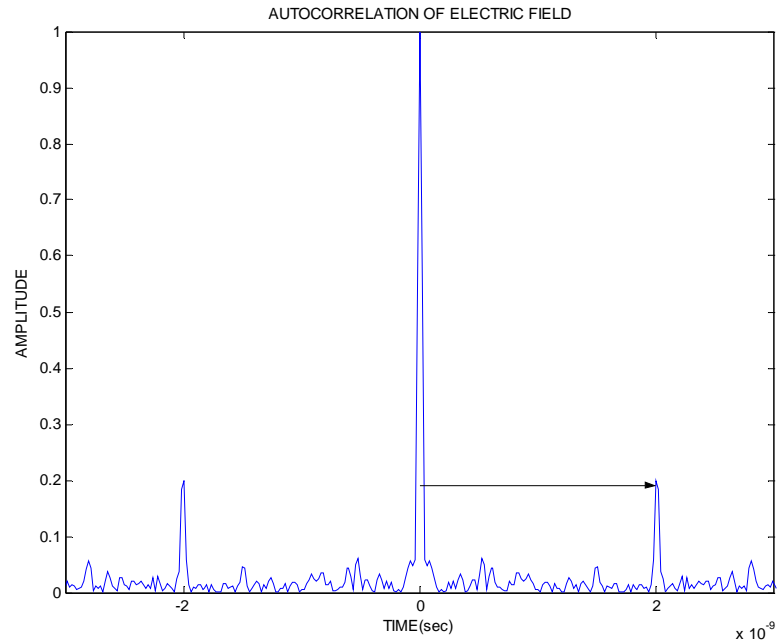


Figure 4.3: Autocorrelation of the electric field for $L_{\text{ext}}=0.30\text{m}$.

The mainlobe width, the poor man's Lyapunov exponent, and the compression bandwidth of the signal are estimated from the autocorrelation of the chaotic field and are shown in Table 4.3. Here the signal's bandwidth is calculated by taking the reciprocal of the main lobe width of the autocorrelation as described in section 2.7.3. Notice that the external cavity length does not have an impact on any of the parameters of the autocorrelation.

Table 4.3: Main lobe width, poor man's Lyapunov exponent (LE) and bandwidth of chaotic field

L_{ext}	Main lobe width	Poor man's LE	Compression Bandwidth
0.05	4.64×10^{-11} sec.	0.4310	21.55GHz
0.10	4.53×10^{-11} sec.	0.4415	22.07GHz
0.15	4.52×10^{-11} sec.	0.4424	22.12GHz
0.20	4.47×10^{-11} sec.	0.4474	22.37GHz
0.25	4.57×10^{-11} sec.	0.4376	21.88GHz
0.30	4.52×10^{-11} sec.	0.4492	22.12GHz

The power spectrums of the electric field for an external cavity lengths of $L_{ext}=0.05\text{m}$, 0.15m , and 0.30m are shown in Figures 4.4, 4.5 and 4.6, respectively. In the three cases the bandwidth of the power spectrum is comparable.

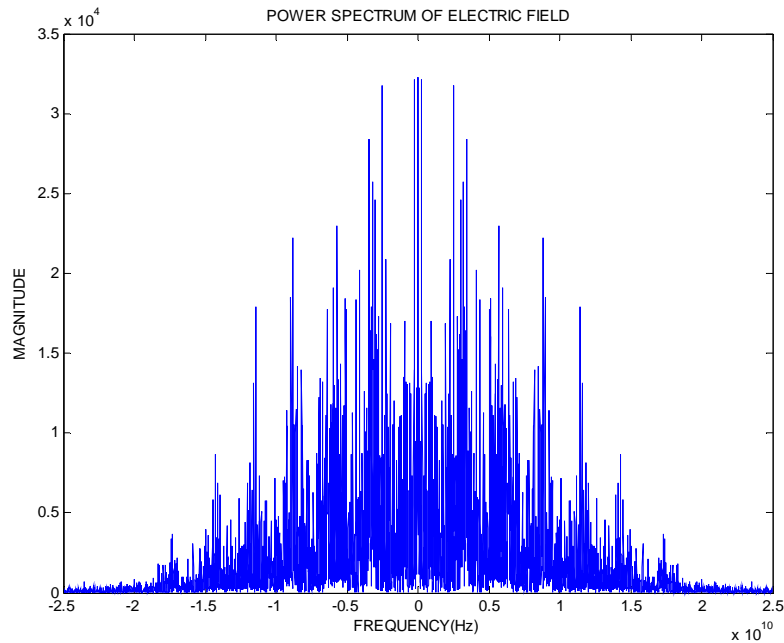


Figure 4.4: Power spectrum of electric field for $L_{ext}=0.05\text{m}$.

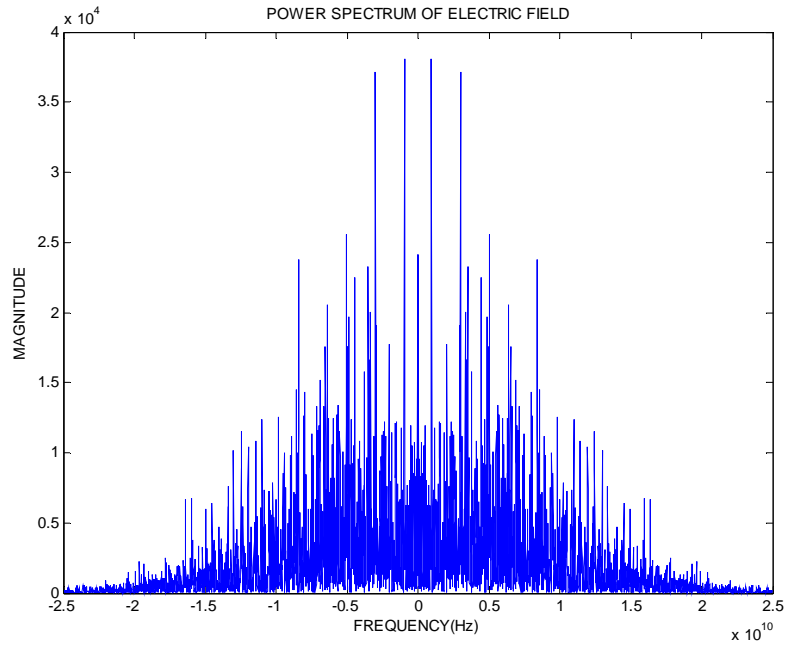


Figure 4.5: Power spectrum of the electric field for $L_{\text{ext}}=0.15\text{m}$.

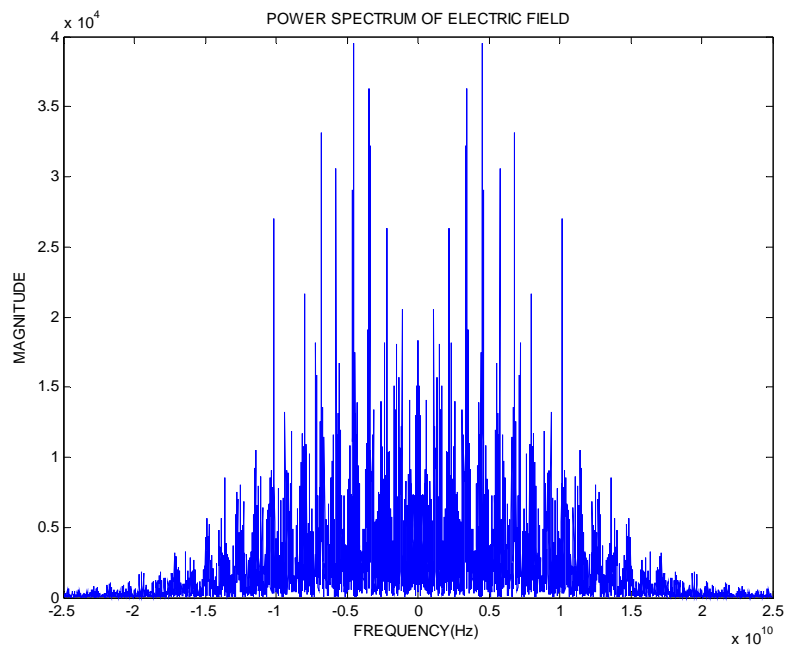


Figure 4.6: Power spectrum of the electric field for $L_{\text{ext}}=0.30\text{m}$.

4.4 Autocorrelation and Power Spectrum for Variable Feedback Level

In the previous section, the effect of varying the external cavity length on the autocorrelation and the power spectrum was analyzed. However, we are also interested in analyzing the effect of the feedback level on the autocorrelation and the power spectrum of the signal.

Thus, the autocorrelation of the chaotic signal is obtained for different feedback levels in the chaotic regime and for an external cavity length of $L_{\text{ext}}=0.30\text{m}$. In Figure 4.7 the normalized autocorrelation of the electric field is shown for a feedback level $\eta=0.02$, which corresponds to the lower threshold of the chaotic regime. In this case, the highest side lobe level is 46.6 percent of the peak value.

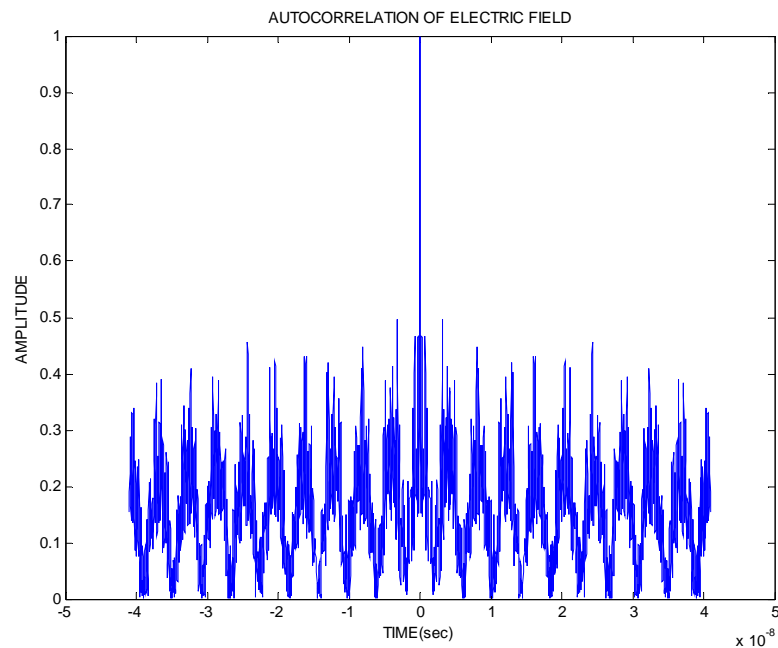


Figure 4.7: Autocorrelation of the electric field for $\eta=0.02$.

A close up of the autocorrelation near the mainlobes is shown in Figure 4.8. Notice that the sidelobe levels are extremely high which indicates that the signal does not decorrelate with time. In addition, some degree of periodicity can be observed. This is consistent with the behavior of the strange attractor that forms a toroid around a steady state orbit.

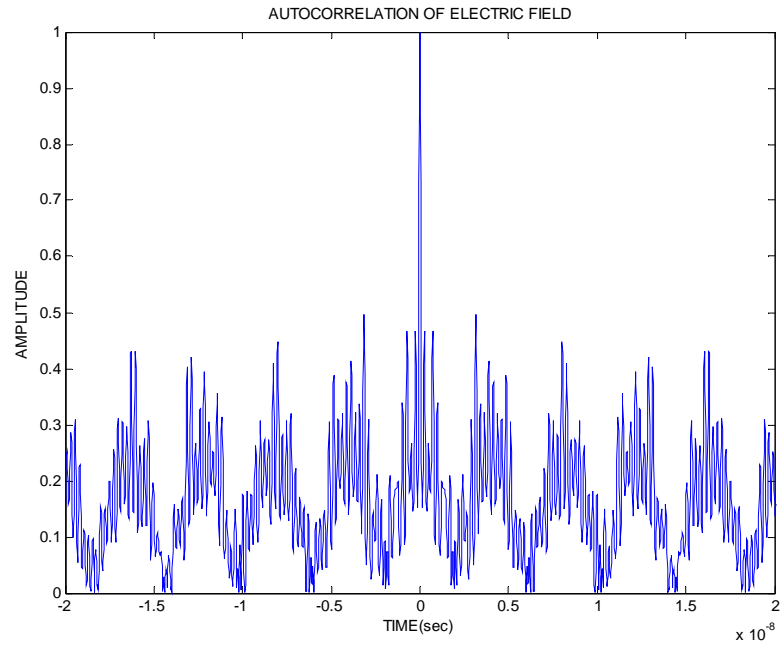


Figure 4.8: Zoom in of the autocorrelation of the electric field for $\eta=0.02$.

Figure 4.9 shows the autocorrelation of the signal for a higher feedback level of 0.05. In this case, the highest side lobe level is 0.1828 and the samples are seen to decorrelate quickly.

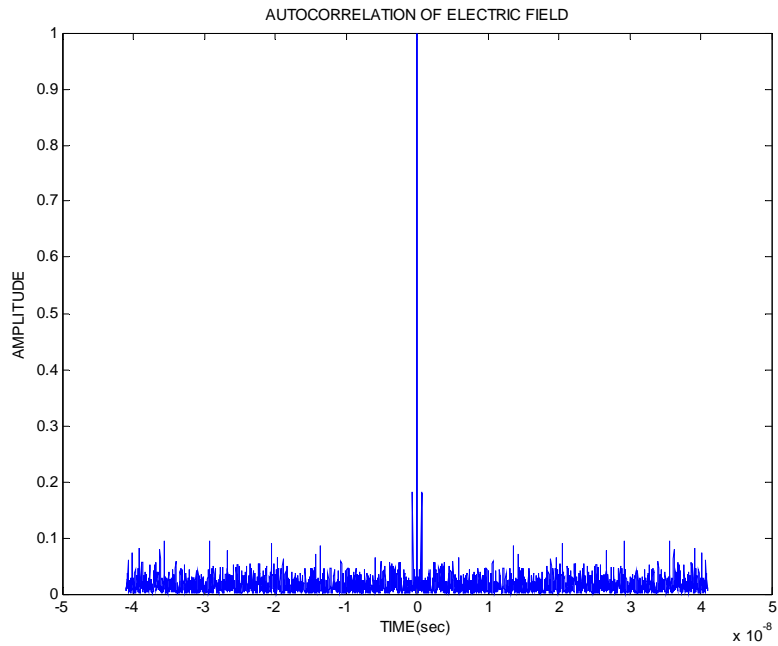


Figure 4.9: Autocorrelation of the electric field for $\eta=0.05$.

A close up of the autocorrelation of the electric field is shown in Figure 4.10, where it can be observed that the autocorrelation has just two sidelobes with high amplitude. The other sidelobes are lower than 5 percent of the peak intensity. The location of these sidelobes depends on the length of the cavity as will be explained below.

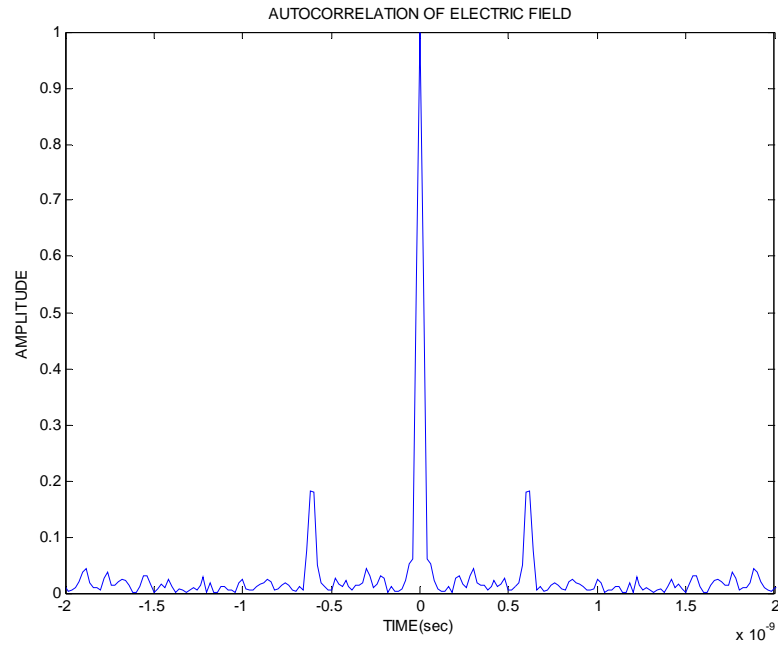


Figure 4.10: Zoom in of the autocorrelation of the electric field for $\eta=0.05$.

Figure 4.11, shows the autocorrelation of the electric field for a feedback level of 0.09, which is the upper limit of the chaotic regime. In this case, the highest side lobe reaches a level of 34 percent. Although the samples decorrelate in time, the autocorrelation has four sidelobes.

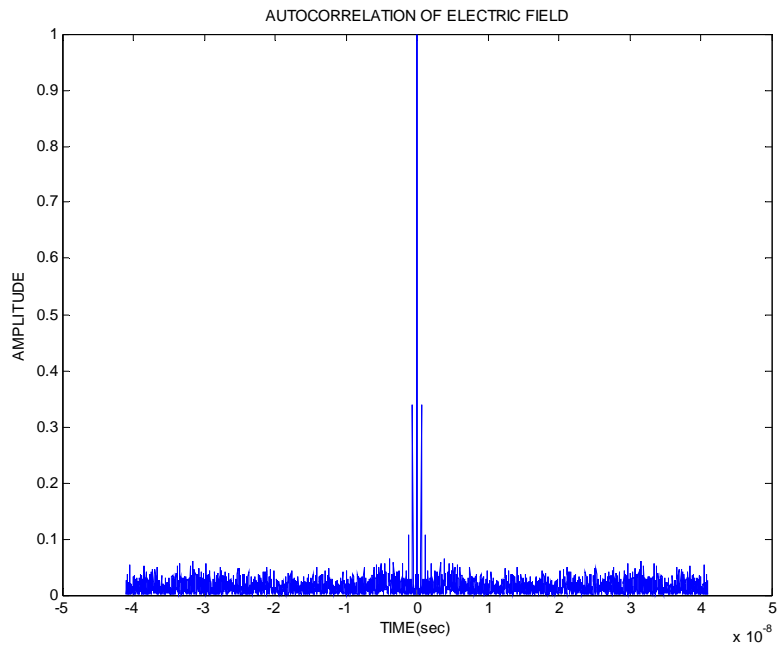


Figure 4.11: Autocorrelation of the electric field for $\eta=0.09$.

Figure 4.12 shows a close up of the autocorrelation of the electric field. In this Figure, four side lobes can be easily distinguished which would indicate that the signal has regained some periodicity.

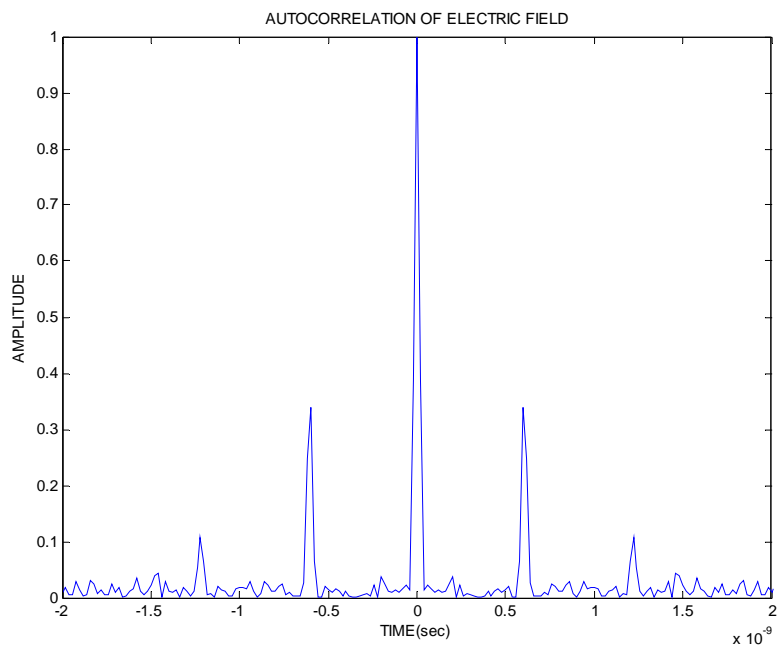


Figure 4.12: Zoom in of the autocorrelation of the electric field for $\eta=0.09$.

Table 4.4 shows the main lobe width and the corresponding compression bandwidth of the chaotic signal for different feedback levels of η .

Table 4.4: Autocorrelation main lobe width, poor man's Lyapunov exponent and bandwidth of electric field for variable η

Feedback level η	Main Lobe Width	Poor Man's LE	Compression Bandwidth
0.02	7.8×10^{-11} sec.	0.2564	12.82GHz
0.03	6.16×10^{-11} sec.	0.3246	16.23GHz
0.04	5.18×10^{-11} sec.	0.3861	19.30GHz
0.05	4.52×10^{-11} sec.	0.4492	22.12GHz
0.06	4.54×10^{-11} sec.	0.4405	22.02GHz
0.07	3.88×10^{-11} sec.	0.5154	25.77GHz
0.08	3.5×10^{-11} sec.	0.5714	28.57GHz
0.09	3.28×10^{-11} sec.	0.6097	30.48GHz

The power spectrum of the electric field for a feedback level $\eta=0.02$ is shown in Figure 4.13. In this case, we observe that the spectrum of the signal is no longer coherent and spreads over a bandwidth of 12.82GHz.

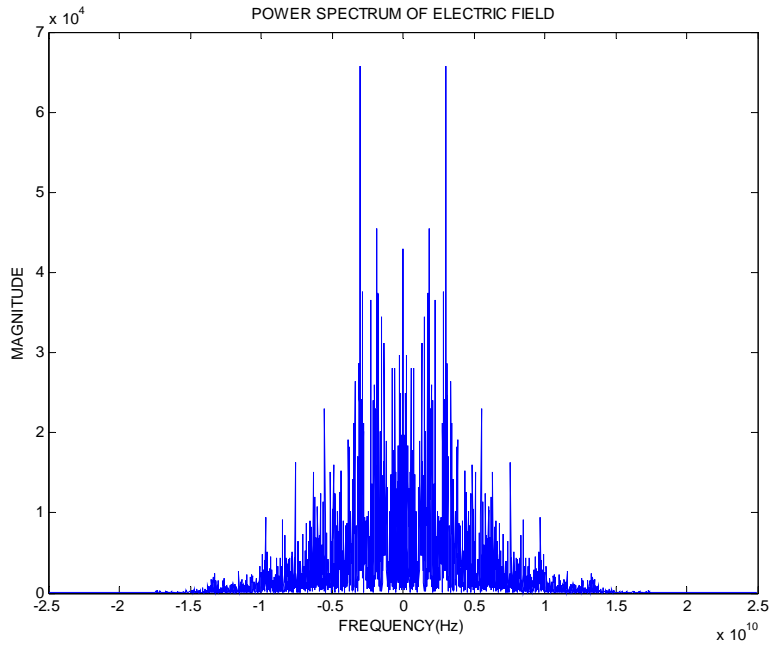


Figure 4.13: Power spectrum of the electric field for $\eta=0.02$.

The power spectrum of the electric field for a feedback level $\eta=0.05$ is shown in Figure 4.14. Although the compression bandwidth is 22.12GHz, which is close to the value in the previous case, the energy is spread more evenly over a wider frequency range.

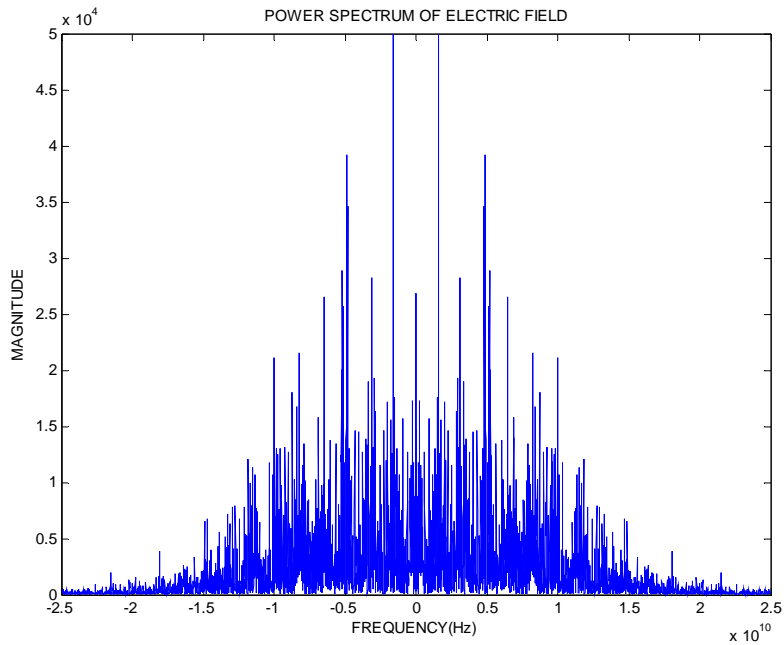


Figure 4.14: Power spectrum of the electric field for $\eta=0.05$

The power spectrum of the electric field for a feedback level $\eta=0.09$ is shown in Figure 4.15. The bandwidth in this case increased up to 30.48GHz by increasing the number of modes in the signal. At this point the laser output has a number of mode lines.

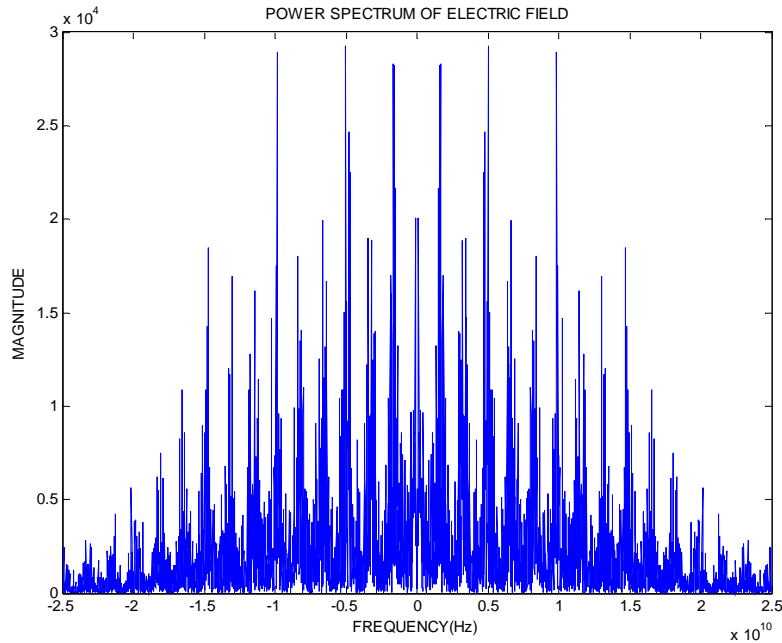


Figure 4.15: Power spectrum of the electric field for $\eta=0.09$

It is clear from these simulations that the spectrum reaches an ideal distribution somewhere near the middle of the range of η . However, the analysis of the spectral distribution alone is insufficient to select the feedback level that gives the best chaotic signal.

4.5 Feedback Level Selection

In this section, we seek additional ways to characterize the chaotic electric field generated by the LADAR system under study. For this purpose we consider the entropy of the field's autocorrelation, the Lyapunov exponent of the field, and the effective bandwidth of its spectrum.

As described in Chapter 2, the entropy is a measure that is used to evaluate the degree of randomness of a variable. For instance, an experiment with a strong bias toward a single value has lower entropy compared to another experiment with a wider distribution of values. Thus, we speculate that an

entropy value can be associated with the temporal autocorrelation of a signal. The faster the autocorrelation dies out with increasing delay, the lower its entropy. Conversely, if the autocorrelation dies out slowly or shows multiple sidelobes, it must have higher entropy.

In contrast, the Lyapunov exponent is used as a measure of divergence of the electric field from its initial conditions. For instance consider two sequences of the electric field with slightly different initial conditions. A high Lyapunov exponent value indicates that the electric field orbits quickly diverge from each other. The third parameter used is the effective (rms) bandwidth of the field. This is obtained by considering the spectral weighing in the strength of the spectral distribution. A large effective bandwidth means that the power of the signal is widely distributed in the frequency domain. Conversely, a lower effective bandwidth indicates that the power is narrowly distributed.

Table 4.5 summarizes the values of the entropy, Lyapunov exponent, and effective bandwidth obtained through simulations of the electric field for multiple feedback levels. For completeness the entropy of the signal sample distribution is included.

Table 4.5: Evaluation of electric field for different feedback levels

η	S(corr)	S(pdf)	LE	SLL	Effective BW
0.01	3.427	5.130	0.2212	0.466	3.23GHz
0.02	1.194	5.517	0.2956	0.145	4.98GHz
0.03	1.114	5.965	0.2843	0.171	6.67GHz
0.04	0.839	6.058	0.3142	0.175	7.74GHz
0.05	0.742	6.210	0.3281	0.183	8.38GHz
0.06	0.767	6.229	0.3107	0.227	8.35GHz
0.07	0.851	6.298	0.3046	0.282	9.30GHz
0.08	0.929	6.318	0.3223	0.315	10.0GHz
0.09	0.862	6.409	0.3624	0.340	10.4GHz

From previous sections, we found that the autocorrelation of the electric field of the laser output varies as the feedback level varies. Specifically, the sidelobes level increase or decrease depending on

the feedback level. In LADAR applications sidelobes less than -3dB or less than half the peak value are required. In addition, a wideband signal is required in order to obtain higher resolution in the range domain. It was also observed that the bandwidth of the signal changes as the feedback level changes.

The feedback level that produces an optimal signal for LADAR applications is close to $\eta=0.05$. The signal for this feedback level has the lower correlation entropy, a sidelobe level of 0.1828 which is less than half the maximum value, and a root mean square bandwidth of 8.38GHz. In this case, the probability density function has a mean close to zero and is symmetric around the mean.

We also confirmed that the external cavity length does not have much influence on the resulting chaotic waveform. At the same time, the external cavity length does not have a big impact on the power spectrum of the signal. Moreover, the external cavity length has an influence on the major side lobe location on the autocorrelation. We verified that the major sidelobe location is proportional to the external cavity length. As the external cavity length is increased, the major sidelobe increases its distance from the main lobe. For that reason, an external cavity length of $L_{\text{ext}}=0.30$ m was chosen. This gives a better resolution in the range domain.

Chapter 5: LADAR Implementation

5.1 Optical Correlation

The Michelson interferometer discussed in section 2.7.1 can be implemented to obtain the real-time optical cross-correlation of the transmitted and received signal of a LADAR. A schematic of the cross-correlation process is shown in Figure 5.1.

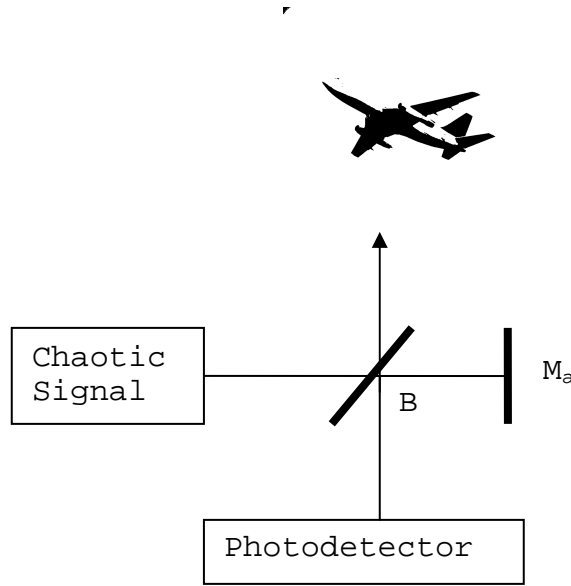


Figure 5.1: Schematic of the cross-correlation of the chaotic field.

The Michelson interferometer is composed of beam splitter B, a mirror M_a and a photodetector. The beam-splitter splits the chaotic signal into two components. The stronger of the beams illuminates the target while the weaker is used for reference. The assumption is that the incident beam forms a local plane wave in the far field and illuminates the entire target. Each “hot” point of the target will contribute to the total power reflected back in the direction of the LADAR. For simplicity let the average delay be τ_0 . In the case of a moving target the reflected signal has a Doppler shift $f_d = 2v/\lambda$; the reflected signal is of the form

$$r(t) = s(t - \tau_0) e^{j2\pi f_d(t - \tau_0)} \quad (5.1)$$

Since the reference signal is reflected first by mirror M_a and then by mirror B, the photodetector responds to the sum of this signal and the echo from the target. Ideally, the photodetector's response should be a current proportional to the magnitude square of $s(t)+\kappa r(t-\tau)$ where κ is proportionality constant that depends on reflectance and transmittance of M_a , and τ is the delay associated with the target's range and the spacing between B and M_a . However, the photodetector has a finite time response that only captures slow frequencies. The net effect of this low pass filtering process is to produce a current that is proportional to the cross product $\kappa s(t)r(t-\tau)$ integrated over a finite amount of time, giving as a result the cross-correlation of the electric field:

$$R_s(\tau) = 2\kappa \int s(t)r^*(t-\tau)dt \quad (5.2)$$

Notice that this is a scaled version of the ambiguity function of the reference signal $s(t)$. To obtain R_s as a function of the delay τ , the distance between B and M_a is changed electromechanically. Hence, we simulate the response of the interferometer as equation 5.2 and drop the proportionality constant.

5.2 Ambiguity function

Recall that the optimized chaotic signal in the previous chapter was obtained for $L_{\text{ext}}=0.30\text{m}$ and $\eta=0.05$ by using the electric field of the laser output. These parameters are used to generate a sequence of $N=1000$ samples. The ambiguity surface of the optimized chaotic signal is shown in Figure 5.2 and a zoom is shown in Figure 5.3. Doppler steps of a fraction of the Doppler resolution are used in the simulation. On average the sidelobes in the range delay axis have a relative magnitude of $10\log_{10}(1/N)$ with respect to the peak, which in this case is approximately -30dB. This level is used to define the pedestal of the thumbtack ambiguity surface. The sidelobes along the range delay peak are symmetric to the origin and have an intensity of approximately -10 dB. Along the Doppler axis, the sidelobes adjacent to the main lobe have the theoretical value of -13 dB. In this case, the sidelobes in the Doppler axis is approximately -13 dB.

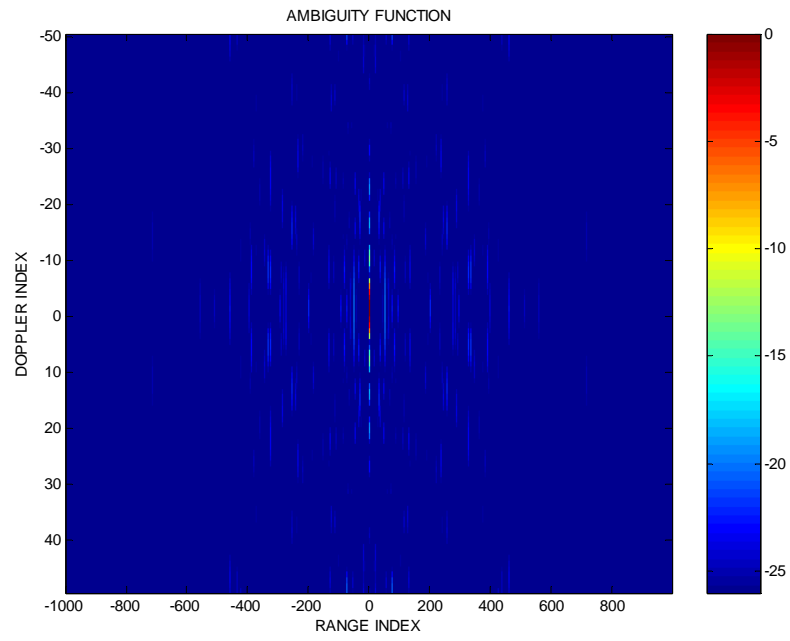


Figure 5.2: Ambiguity function of the electric field of laser output.

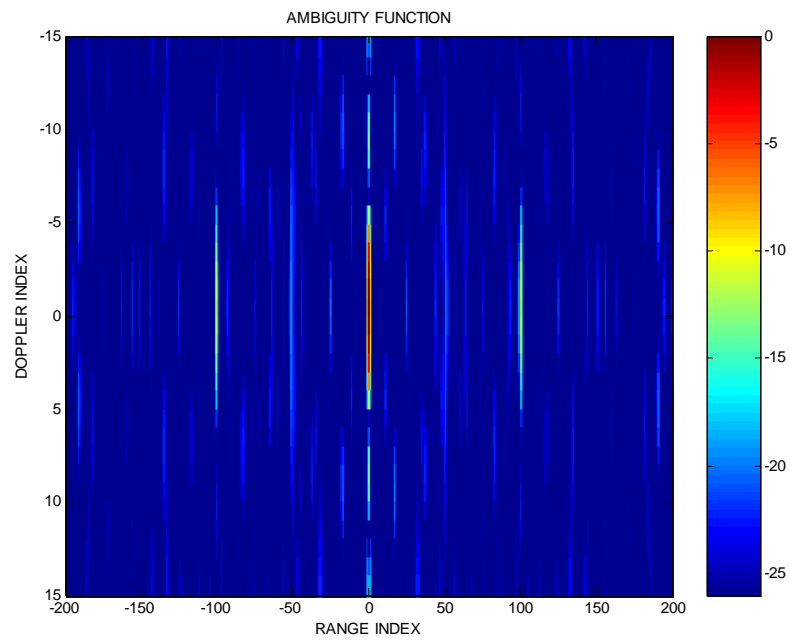


Figure 5.3: Zoom in of the ambiguity function of the electric field.

By using the intensity of the laser output, the ambiguity function was obtained for comparison for a feedback level of 0.05 and an external cavity length of 0.30m. In Figure 5.4, the ambiguity function of the intensity is shown. In Figure 5.5 a zoom in of the ambiguity function is shown. The range delay

peak is approximately -7 dB. However, a more peaked ambiguity function was obtained with the electric field. The ambiguity function of the intensity many sidelobes exist as can be observed in the next Figure.

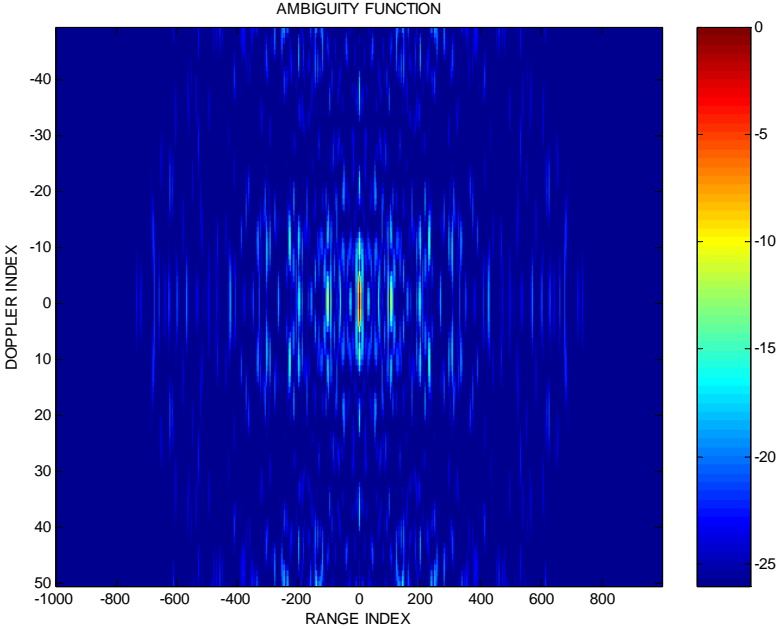


Figure 5.4: Ambiguity function of intensity of laser output.

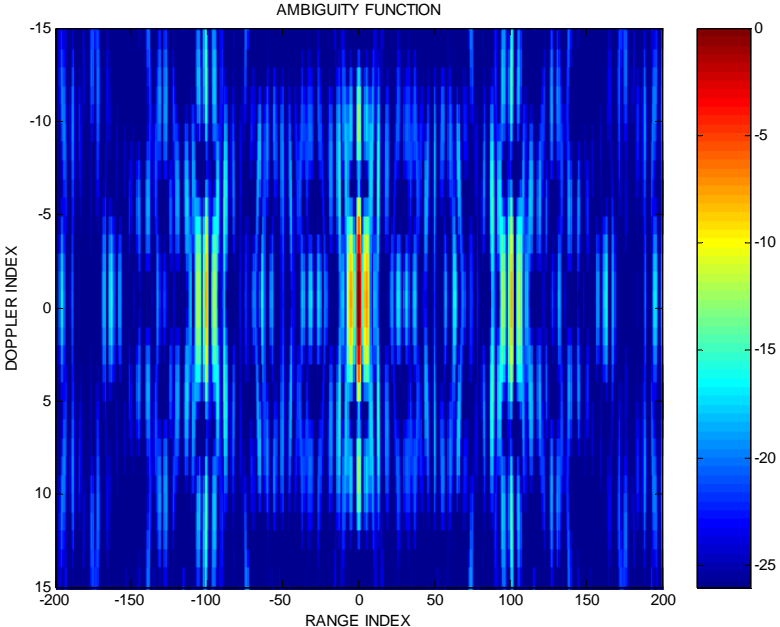


Figure 5.5: Zoom in of ambiguity function of intensity.

The ambiguity function of a random field obtained from 1000 samples is shown in Figure 5.6. In this case the sidelobe levels in the range axis have an average value of -30dB. The side lobe levels in the Doppler axis have a level of -15dB. A zoom in of the ambiguity function is shown in Figure 5.7.

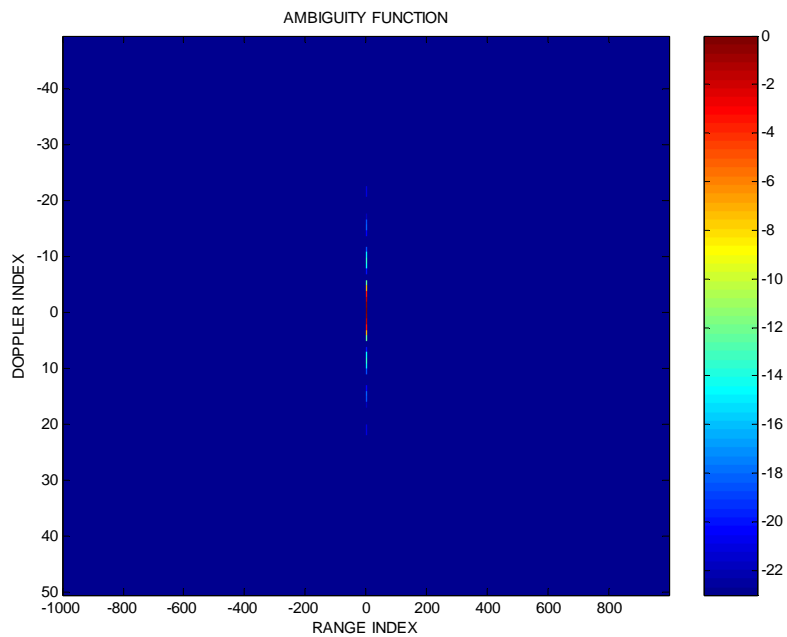


Figure 5.6: Ambiguity function of the random signal.

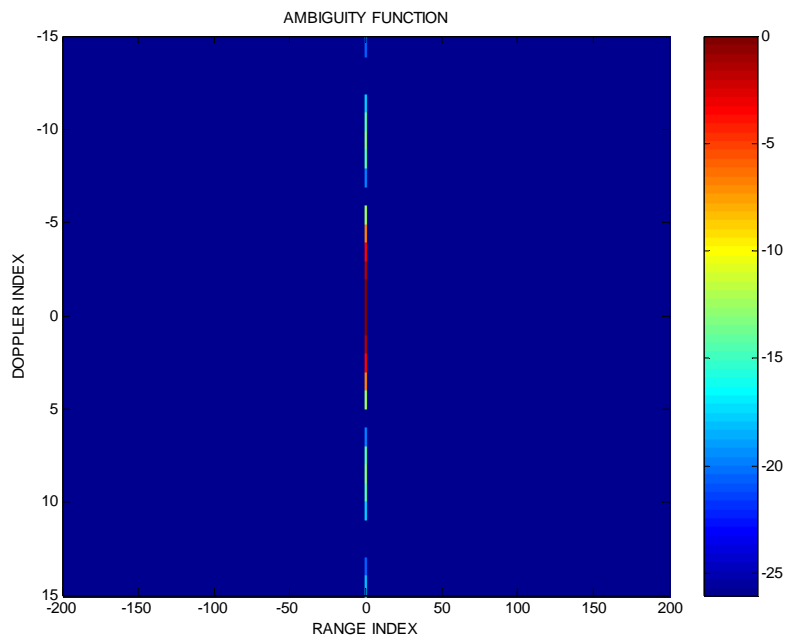


Figure 5.7: Zoom in of the ambiguity function of the random signal.

The entropy of the ambiguity function is obtained using equation 2.37. Elsewhere, the entropy of the ambiguity function has been used as a focal quality indicator. The image of a hot spot is perfectly focused when its entropy is a minimum. Table 5.1 shows the entropy of the ambiguity function for $L_{\text{ext}}=0.30\text{m}$ and different feedback levels. The lower ambiguity function entropy is obtained for $\eta=0.05$. This means that the image is of higher quality when this feedback level is used.

Table 5.1: Entropy measurement for variable feedback level

Feedback Level	Entropy of ambiguity function $S\chi$
0.02	4.964
0.03	4.923
0.04	4.933
0.05	4.897
0.06	4.929
0.07	4.908
0.08	4.905
0.09	4.901

5.3 Target Imaging

In order to simulate a more realistic target, an aircraft with multiple hot spots is chosen. The echo of the target is modeled as a coherent sum of n reflections:

$$r(t) = \sum_{i=1}^n s(t - \tau_i) e^{j2\pi f_{di}(t - \tau_i)} \quad (5.3)$$

where n is the number of scatter points, τ_i is the delay associated with each scatter point, f_{di} is the Doppler shift associated with each hot spot. For simplicity, the radar cross section of all the hot spots is assumed to be the same and independent of viewing angle. The signature of the target was obtained by

using a bank of matched filters as it is shown in Figure 5.8. The received signal $r(t)$ is passed through a bank of m filters. Each filter is a matched filter with a frequency f_d .

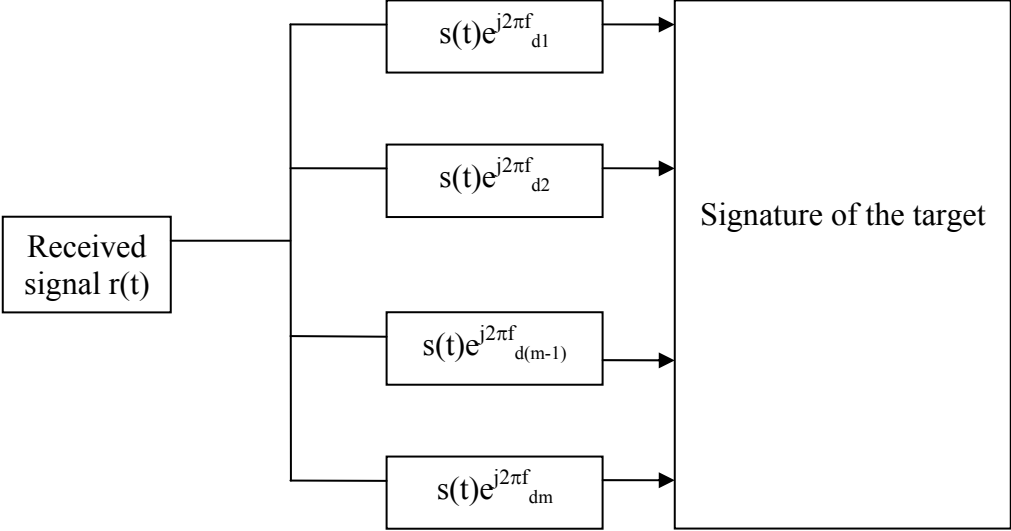


Figure 5.8: Block diagram of bank of matched filters.

The resulting image in the range and Doppler plane is shown in Figure 5.9. In this Figure, 12 hot spots were used to obtain the image of a Boeing 777. A total number of 500 samples of the electric field were used to obtain the signature of the target.

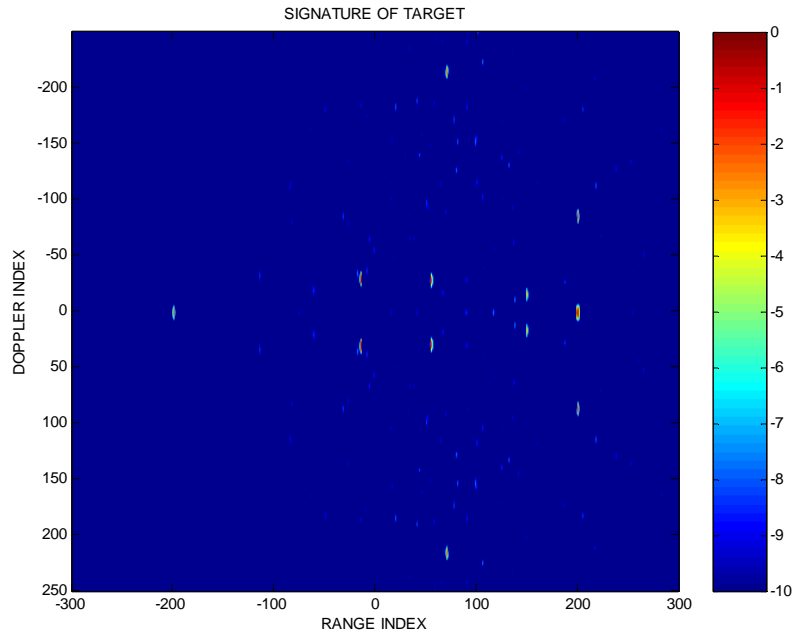


Figure 5.9: Image of the target in the range and Doppler plane by using the electric field.

For comparison, the signature of the target by using the intensity of the laser output is shown in Figure 5.10.

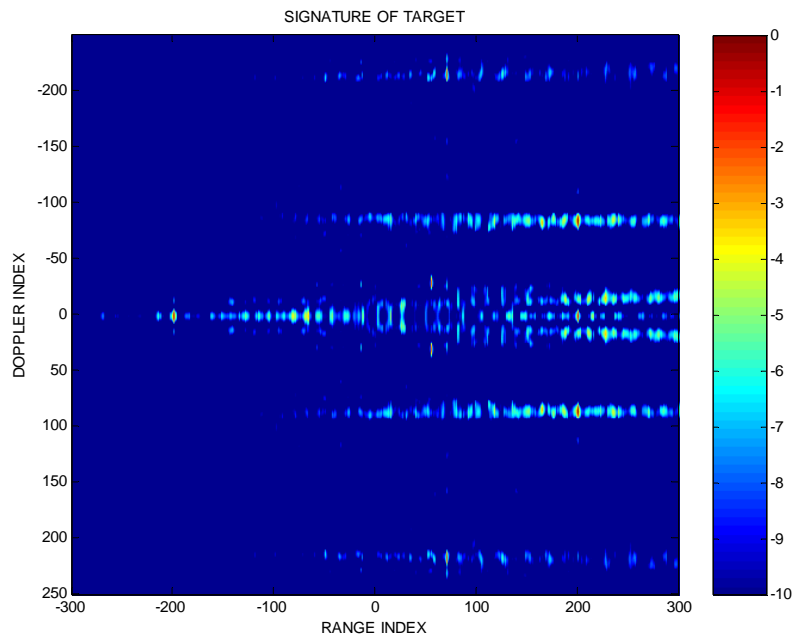


Figure 5.10: Image of the target in the range and Doppler plane by using the laser intensity.

Chapter 6: Conclusion

Chaotic dynamics are commonly modeled as complex nonlinear multivariable systems. By solving the differential equations that govern one such system, a deterministic signal can be generated with an apparent random behavior in time and frequency that depends on a set of control parameters. However, the time-frequency analysis alone, which includes a study of the autocorrelation and spectrum of the signal, can not be used to conclude that these signals are, in the strict sense, chaotic. In this dissertation, a complete characterization was performed for the electric field of a semiconductor laser driven into chaos via optical feedback, which is modeled as a three dimensional system. The characterization of this (Lang-Kobayashi) system included pseudo phase maps, attractors and Lyapunov exponent calculations. In addition, a statistical analysis of the electric field was performed to illustrate that the electric field is indeed ergodic.

In the literature, attention is often placed on the intensity of the laser output. In doing this, the chaotic nature of the phase of the electric field is ignored. Through this research, it was demonstrated that the baseband representation of the electric field of the system includes both amplitude and phase information that, when used for LADAR purposes, can improve the performance of the system. This was shown by analyzing the ambiguity function of the intensity of the laser output and the electric field of the laser output as a function of time delay and Doppler shift. For an accurate description of the process, the ensemble average of the ambiguity function was obtained by introducing small changes in the initial conditions of the chaotic system. It was found that the magnitude of ambiguity function of the laser's electric field formed a nearly ideal "thumbtack" surface with sidelobes averaging a magnitude of $-20 \log(N)$ dB where N is the number of iterations of the electric field used in the computations. This result is in sharp contrast with the sidelobe level obtained by computing the ambiguity function of the laser intensity, which averaged a magnitude of $-10 \log(N)$ dB. In addition, the range resolution achieved by compressing a signal proportional to the electric field was of the order of 1 mm with a compression bandwidth of the order of 10 GHz. This is an improvement of approximately 50% compared to the range resolution attainable by compressing a signal proportional to the intensity of the laser beam. It was also demonstrated that processing of the chaotic electric field has a real potential for

use in range-Doppler imaging applications given that the dynamic range of the responses that can be mapped spans nearly 30 dB with the processing of as few as 1000 samples per correlation. To illustrate this possibility, the signature of a Boeing 777 with twelve hot spots of identical reflectance was simulated and processed via matched filtering. The resulting imagery leaves no doubt that a clear image of the airplane can obtain by processing the electric field. The image obtained by processing the intensity of the laser is affected by higher sidelobes and reduced resolution.

Future work in this area will include the analysis of the Lang-Kobayashi system in presence of additive and phase noise. Specifically, the plan is to perform the optimization of the signal and obtain range and Doppler information including Langevin noise, thermal noise and shot noise. Also, the idea of performing a smart optimization using genetic algorithms is interesting to pursue. Yet another topic for study is the possibility of synchronizing the chaotic field of the two distinct lasers that are needed to form a bistatic LADAR.

References

- [1] N. Holonyak Jr., Semiconductor alloy lasers-1962, IEEE Journal of Quantum Electronics, vol. 23, Issue: 6, pp. 684- 691, Jun 1987.
- [2] Roy Lang and Kohroh Kobayashi, "External Optical Feedback Effects on Semiconductor Injection Laser Properties", IEEE Journal of Quantum Electronics, vol. QE-16, NO. 3, 1980.
- [3] Lenstra, B. H. Verbeek, and A. J. Den Boef, "Coherence Collapse in Single Mode Semiconductor Lasers due to Optical Feedback", IEEE Journal of Quantum Electronic, vol. QE-21.
- [4] C. Masoller, "Coexistence of attractors in a laser diode with optical feedback from a laser external cavity", Physical Review, vol. 50, NO. 3, 1994.
- [5] Jun Ye, Hua Li, and John G. McInerney, "Period-doubling route to chaos in a semiconductor laser with weak optical feedback", Physical Review, vol. 47, NO. 3, 1993.
- [6] Hua Li, Jun Ye, John G. McInerney, " Detailed Analysis of Coherence Collapse in semiconductor lasers", IEEE Journal of Quantum Electronic, vol. 29, NO. 9, 1993.
- [7] Noriyuki Kikuchi, Yun Liu, and Junji Ohtsubo, "Chaos control and Noise suppression in external cavity semiconductor lasers", IEEE Journal of Quantum Electronics, vol. 33, NO. 1, 1997.
- [8] Jesper Mork, Bjarne Tromborg, and Jannik Mark, "Chaos in semiconductor lasers with optical feedback: theory and experiment", IEEE Journal of Quantum Electronics, Vol. 28, NO. 1, 1992
- [9] Shawn D. Pethel, Ned J. Corron, "Chaotic LADAR", App. Phys. Lett. 78, 2001.
- [10] Fan-Yi Lin, Jia-Ming Liu, Chaotic Lidar, IEEE Journal of Quantum Electronics, vol. 10, NO.5, 2004
- [11] John Banks, valentine Dragan, Arthur Jones, *Chaos: A Mathematical Introduction*, Cambridge Press, New York, 2003.
- [12] Michael Peter Kennedy, Riccardo Rovatti, Gianluca Setti, Eds., *Chaotic Electronics in Telecommunications*, CRC Press, 2000.
- [13] Benjamin C. Flores, Berenice Verdin, Gabriel Thomas, "Parameter Selection of discrete chaotic maps for improved FM ambiguity surface statistics", SIAM conference, May 2005.
- [14] Benjamin C. Flores, Berenice Verdin, " Wideband Radar Imaging using chaotic based Gaussian frequency modulation", SPIE, April 2006.
- [15] Benjamin C. Flores, Gabriel Thomas, "Chaotic Signals for wideband radar imaging", Proc. SPIE, vol. 4727, 2002
- [16] Joachim Sacher, Dieter Baums, Petter Panknin, "Intensity instabilities of semiconductor laser undercurrent modulation, external light injection and delayed feedback", Physical Rev. , vol. 45, NO. 3, 1992
- [17] Tang Shuo, Liu Jiaming, "Nonlinear dynamics and applications of semiconductor laser with optoelectronic feedback", Proc. SPIE, Vol. 4646, pp. 333-541, 2002
- [18] Junji Ohtsubo, *Semiconductor lasers: Stability, Instability and Chaos*, Springer, 1 edition, 2005
- [19] John Gomar, *Optical Communication Systems*, Prentice Hall, London, 1984.

- [20] Jurgen R. Meyer-Arendt, Introduction to Classical and Modern Optics, second edition, Prentice Hall, New Jersey, 1994.
- [21] Robert G. Harrison, Dhruba J. Biswas, “Chaos in light”, Nature Publishing Group, vol. 312, May 1986
- [22] Ray, William, “Stochastic and deterministic dynamics in a semiconductor laser with optical feedback”, Dissertation, Department of Physics, 2006.
- [23] G H M van Tarwijk and D Lenstra, “Semiconductor lasers with optical injection and feedback”, Quantum Semiclass, Opt 7, 1985
- [24] Pascal, Besnard, B. Meziane, Guy Michel, “Feedback phenomena in a semiconductor laser induced by distant reflectors”, IEEE Journal of Quantum Electronics, vol. 29, May 1993.
- [25] Shinsuke Rukushic, Shu-Ying YE and Junji Ohtsubo, “Relaxation oscillation enhancement and coherence collapse in semiconductor lasers with optical feedback”, Optical Review, vol. 6, NO. 4, 1999.
- [26] P. M. Alsing, V. Kovanis and A. Gavrielides, “Lang and Kobayashi Phase Equation”, Physical Review, vol. 53, NO. 6.
- [27] Julien Clinton Sprott, Chaos and Time Series Analysis, Oxford University Press, Oxford, 2003.
- [28] Adrzej Lasota, Michael C. Mackey, Chaos, Fractals, and Noise Stochastic Aspects of Dynamics, Springer-Verlag, New York, 1994.
- [29] Mark A. Richards, Fundamentals of Radar Signal Processing, McGraw-Hill, New York, 2005.
- [30] Bassem R. Mahafza, Radar Systems Analysis and Design using MATLAB, second edition,
- [31] Shannon, C.E. A Mathematical Theory of Communication, Bell Syst. Tech. J., vol. 27, 1948, pp.379–423.
- [32] Jae Sok Son, Gabriel Thomas, Benjamin C. Flores, Range-Doppler radar imaging and motion compensation, Artech House, Boston, 2001, pp. 20-24.
- [33] Albert V. Jelalian, Laser Radar Systems, Artech House, Boston, 1992.
- [34] Hermann A. Haus, Waves and Fields in Optoelectronics, Prentice-Hall, New Jersey, 1984.
- [35] Hector Ochoa, Radar signal analysis for high velocity targets using the electromagnetic field tensor and the lorentz transformation, Dissertation, University of Texas at El Paso, 2007.
- [36] Hector Garces, Wideband chaotic signal analysis and processing, Dissertation, University of Texas at El Paso, 2007

Vita

Berenice Verdin was born on February 7, 1981 in El Paso, TX to Maria and Luis Verdin. She graduated with a BS degree in Electrical Engineering from the University of Texas at El Paso in spring of 2003. As an undergraduate, she was selected to participate in the Research Experience for Undergraduates (REU) program. As a graduate student, she was involved in a project funded by the Army Research Laboratories. She presented her research results at the UTEP Student Research Expo, the UMET Undergraduate Research Symposium, and the SPIE Symposium on Defense and Security. She also presented her research work to the National Science Board and the Director of the National Science Foundation. She earned her Master of Science in Electrical Engineering in August 2005. As a PhD student she worked on a project sponsored by Army Research Laboratories. She presented her research results on SPIE Symposium Photonics + Applications. She earned her PhD in Electrical and Computer Engineering in August 2009.

Permanent address: 512 Fortenberry
El Paso, TX, 79928

This dissertation was typed by Berenice Verdin.